Transition Metal Dichalcogenide TiS2 Prepared by Hybrid Atomic Layer Deposition/Molecular Layer Deposition: Atomic-Level Insights with In Situ Synchrotron X-ray Studies and Molecular Surface Chemistry

P. Younes, E. Skopin, M. Zhukush, L. Rapenne, H. Roussel, N. Aubert, L. Khrouz, C. Licitra, C. Camp, Marie-Ingrid Richard, et al.

Transition Metal Dichalcogenide TiS2 Prepared by Hybrid Atomic Layer Deposition/Molecular Layer Deposition: Atomic-Level Insights With in situ Synchrotron X-ray Studies And Molecular Surface Chemistry.

Journal:	*Chemistry of Materials*
Manuscript ID	cm-2022-02369w.R1
Manuscript Type:	Article
Date Submitted by the Author:	n/a
Complete List of Authors:	ABI YOUNES, Petros; Universite Grenoble Alpes, Skopin, Evgeniy ; Laboratoire des technologies de la microelectronique Zhukush, Medet; IRCELYON Rapenne, Laetitia; Institut Polytechnique de Grenoble, of Materials Science Roussel, Hervé; Universite Grenoble Alpes, LMGP Aubert, Nicolas; Synchrotron SOLEIL - Beamline SIRIUS, Khrouz, Lhoussain; Ecole normale superieure de Lyon, Laboratoire de Chimie Licitra, Christophe; CEA-Leti CAMP, Clément; C2P2, Richard, Marie-Ingrid; ESRF, Schneider, Nathanaelle; IPVF Ciatto, Gianluca; Synchrotron SOLEIL, experience Gauthier, Nicolas; CEA-Leti Rouchon, Denis; CEA-Leti Quadrelli, Elsje; IRCELYON Renevier, Hubert; Universite Grenoble Alpes, Laboratoire des Matériaux et du Génie Physique, UMR 5628

Transition Metal Dichalcogenide TiS_2 Prepared by Hybrid Atomic Layer Deposition/Molecular Layer Deposition: Atomic-Level Insights With *in situ* Synchrotron X-ray Studies And Molecular Surface Chemistry.

Petros Abi Younes[1,2,*], Evgeniy Skopin[1], Medet Zhukush[3], Laetitia Rapenne[1], Hervé Roussel[1], Nicolas Aubert[5], Lhoussain Khrouz[6], Christophe Licitra[2], Clément Camp[4], Marie-Ingrid Richard[7,8], Nathanaelle Schneider,[9] Gianluca Ciatto[5], Nicolas Gauthier[2], Denis Rouchon,[2] Elsje Alessandra Quadrelli[3,*] and Hubert Renevier[1,*]

[1]LMGP, Univ. Grenoble Alpes, CNRS, Grenoble-INP, Grenoble, France

[2]Univ. Grenoble Alpes, CEA, LETI, F-38000 Grenoble, France

[3]Université de Lyon, IRCELYON, Institut de Recherche sur la catalyse et l'environnement (UMR 5256 CNRS Université Lyon1), 2 av. Albert EINSTEIN, 69100 Villeurbanne, France

[4]Université de Lyon, CP2M, Laboratory of Catalysis, Polymerization, Processes and Materials, UMR 5128 CNRS-UCB Lyon 1-CPE Lyon, Institut de Chimie de Lyon, 43 Bvd du 11 Novembre 1918, 69616 Villeurbanne, France

[5]Synchrotron SOLEIL, Beamline SIRIUS, L'Orme des Merisiers, Saint-Aubin, F-91192, Gif sur Yvette, France

[6]ENSL, CNRS, Laboratoire de Chimie UMR 5182, *ENS Lyon (École Normale Supérieure de Lyon, site René Descartes), 15 parvis René Descartes, 69342 Lyon, France*

[7]Univ. Grenoble Alpes, CEA Grenoble, IRIG, MEM, NRS, 17 rue des Martyrs 38000 Grenoble, France

[8]European Synchrotron Radiation Facility, 71 Avenue des Martyrs, 38043 Grenoble, France

[9]IPVF (UMR 9006), Institut Photovoltaïque d'Ile-de-France, 18 boulevard Thomas Gobert, 91120 Palaiseau, France

** petros.abi-younes@grenoble-inp.fr ; * elsje.quadrelli@ircelyon.univ-lyon1.fr ; * hubert.renevier@grenoble-inp.fr*

23/10/2022 21:26

Abstract

In this work, 2D-material titanium disulfide (TiS_2) film was grown using tetrakis(dimethylamido)titanium and 1,2 ethanedithiol on 100 nm thick amorphous SiO_2/Si substrate. The first step of the process relied on the growth of an amorphous film of Ti amidothiolate by hybrid Atomic Layer Deposition/Molecular Layer Deposition (ALD/MLD) at 50 °C. Such thiolate converted into TiS_2 upon subsequent thermal annealing under H_2(4%)/Ar(96%) at 450 °C. The final lamellar TiS_2 layers tend to be parallel to the substrate surface as observed by transmission electron microscopy and confirmed at a larger scale by x-ray absorption linear dichroism at the Ti K-edge. The crystalline quality of the resulting films was assessed by Raman scattering. Angle-resolved x-ray photoelectron spectroscopy and hard x-ray photoelectron spectroscopy confirmed the stoichiometry of the TiS_2 layer.

Repetitive and self-limiting growth behavior on the SiO_2/Si substrate was displayed from the early stages of the growth using *in situ* synchrotron radiation yielding the Ti and S x-ray fluorescence, *in situ* ellipsometry and x-ray reflectivity. Modeling the initial ALD and MLD half-cycles on high-surface-area silica beads afforded characterization by more analytical techniques and provided insights to the growth chemistry that agreed with observations on SiO_2/Si substrate.

Four-point probe resistivity measurements and spectroscopic ellipsometry strongly suggest that the thin films grown on SiO_2/Si substrates behave as heavily doped semiconductors.

1. Introduction

2D-materials, especially Transition Metal Dichalcogenides (TMDC)[1], have received considerable attention recently since emerging as a class of exceptional materials with many potential applications (supercapacitors, batteries, electronics and opto-electronics, flexible electronics, …)[2–4]. TMDCs show unique thickness-dependent properties such as the modulation of the bandgap transition value with the number of 2D layers.[5] Titanium disulfide, TiS_2, which consists of S-Ti-S layers separated by van der Waals gaps, is among the several interesting lamellar TMDC to be investigated for emerging devices: thin TiS_2 is more efficient than bulk material for new supercapacitor electrodes,[6] for low resistivity layered materials enabling the formation of intercalation compounds for rechargeable batteries[7], or as new hybrid TiS_2-based material to be deposited with organic intercalation[8,9]. The TiS_2 layer number/thickness, along with its stoichiometry critically define its semimetal or semiconductor nature[10].

To date, most investigations of TMDC, there included TiS_2, are performed on flakes produced by mechanical exfoliation of bulk crystals. As these are not suited for large-scale applications, methods to deposit uniform high-quality films of accurately controlled thickness on large area are needed to allow full deployment of TMDC materials. While most strategies are based on Chemical Vapor Deposition (CVD), Physical Vapor Deposition (PVD) methods, or chalcogenization of metal or metal oxides,[11,12] Atomic Layer Deposition (ALD) - a gas-phase deposition technique based on sequential, self-limiting surface reactions - appears better adapted to obtain conformal film growth with precise thickness level control, good reproducibility and homogeneity over the substrate area.[13] ALD is already used to

deposit ultrathin films, but the anisotropy of TMDC coupled with the extreme thinness required brings about new challenges, and despite several efforts, the deposition of as-deposited crystalline TMDC remains difficult, possibly necessitating post-annealing steps or chalcogenization of ALD-grown transition metal oxides. [14–18]Among the complicating factors is the co-occurrence of growth and crystallization during the ALD process which becomes particularly limiting when a pre-determined crystal orientation is required. The use of specific crystalline substrates with adequate lattice parameters is a possible strategy to overcome this latter problem. Another approach, which has a larger substrate scope, and is presented herein, is to completely dissociate deposition and crystallization. Such possibility can be accessed by combining the use of organic precursors during the ALD process (such as for example, alcohols, ROH -R being a generic organic fragment- rather than H_2O as oxygen source). The presence of the organic chemical residues prevents the crystallization during the growth of the hybrid inorganic-organic thin film (metalcones in the examples just mentioned [13,19]) at low temperatures. A subsequent treatment (typically annealing which induces loss of most of the organic fragment) leads to the crystallization of the mineral phase.[20,21] For instance, the combination of such organic precursor-based ALD approach — which is called herein Atomic Layer deposition/Molecular Layer Deposition (ALD/MLD)[19] — and post-annealing step allowed to control the porosity of Al_2O_3 thin films,[22] as well as the crystallinity, composition, and electrochemical properties of SnO/SnO_2,[23] TiO_2, and V_2O_5.[24] In the field of TMDC, the authors have demonstrated the value of replacing H_2S, the usual molecule used for sulfide phases growth by ALD, with the MLD precursor 1,2-ethanedithiol (EDT, $HSCH_2CH_2SH$) to obtain, after annealing, atomically thin MoS_2– based layers oriented parallel the substrate, [25] with residual

carbon content similar to an organic precursor-free plasma-enhanced-ALD (PE-ALD) process to MoS_2.

The material of interest here is TiS_2. In the literature, TiS_2 has been synthesized by different growth techniques such as Chemical Vapor Deposition (CVD),[26–31] chemical exfoliation method[32], wet chemical synthesis[33], and the ALD reports remain scant.[2,7,33-37] The first ALD growth of TiS_2, reported in 2007 by Pore *et al*., was grown from $TiCl_4$ and H_2S as titanium and sulphur precursors.[7] Since then, alternative Ti (tetrakis(dimethylamido)titanium, TDMAT)[35] and S (H_2S plasma) [38] sources have been considered as well as two-step strategy (sulfurization of PEALD-TiN thin films).[37] In all cases, the material growth and properties appear strongly dependent on the nature of the substrate and no high-quality ultrathin layered materials could be obtained.[2,7,34–36] Besides, only few applications of ALD TiS_2 thin films are reported (photo-harvesting material, Li^+/Na^+ intercalation, CO_2 reduction reaction), and the challenge of producing ultrathin lamellar TiS_2 remains.

Herein, we consider a novel approach to generate ultrathin lamellar TiS_2-based thin films even on a non-epitaxial substrates such as thermal silicon oxide, which is widely used in microelectronics. The novel approach corresponds to combining an ALD step from TDMAT with a MLD step from EDT (as a safer alternative to highly toxic H_2S) to generate an amorphous hybrid organic-inorganic Ti-thiolate material, with a subsequent annealing treatment at a mild temperature (lower than 450 °C), which leads to a successful in-plane crystallization (see **Scheme 1**). The self-limiting nature of the surface reactions that are necessary to ensure the uniformity, conformality, scalability, and repeatability of the process, are assessed by several advanced techniques coupling, *inter alia*, *in situ* X-ray based monitoring

of the process and chemical modeling on high-surface area silica that collectively lead to a deep understanding of the process.

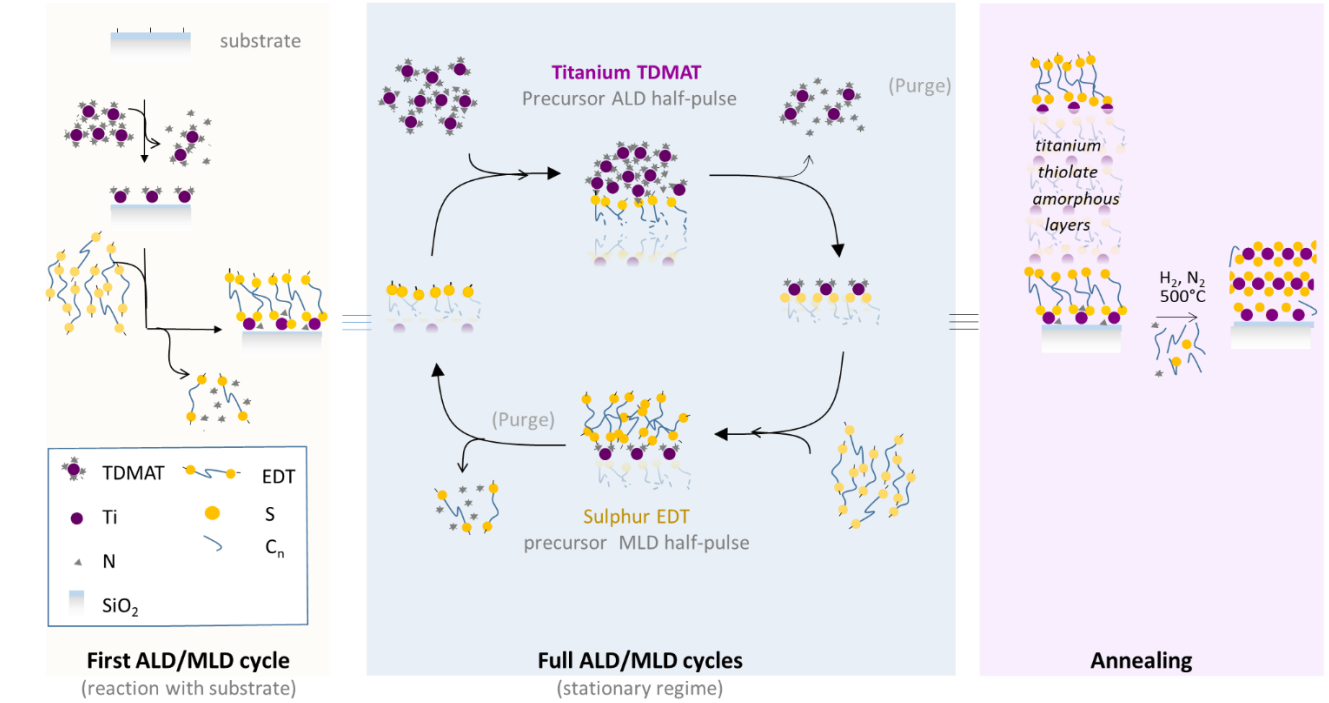

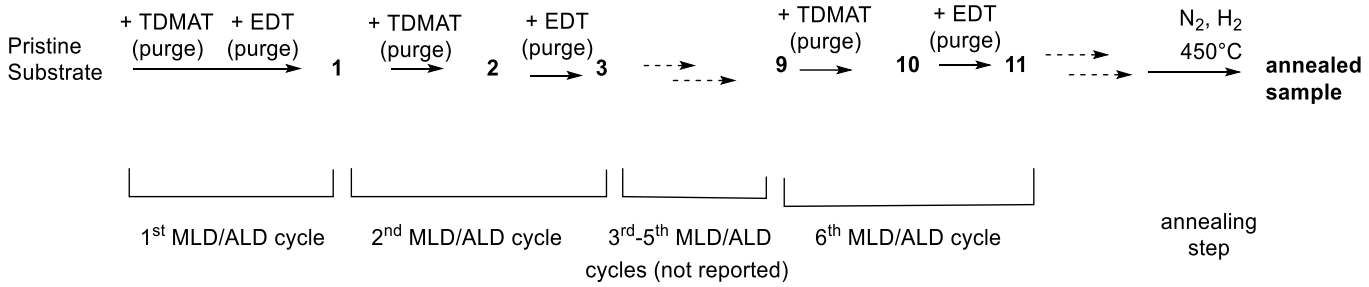

Scheme 1: Schematic overview of the ALD/MLD step (blue background) and annealing step (pink background) of the overall process to TiS_2 reported here and numbering scheme adopted for the silica-supported solids of the modeling studies.

2. Experiments

2.1. Starting chemicals

Tetrakis(dimethylamido)titanium (IV), TDMAT (CAS number: 3275-24-9, 99.999% purity) and ethylenedithiol, EDT (CAS number: 540-63-6, assay greater than 99%) were purchased from Merck™. The reference TiS_2 sample was purchased from Merck™ (CAS number: [12039-13-3]). All reactions among molecular precursors or between molecular precursors and silica beads were carried out under a controlled argon atmosphere using Schlenk glassware and glovebox. General preparing procedure and materials as well as equipment are detailed in the Supplementary Information (SI).

2.2. Modeling of ALD/MLD growth on silica-terminated silicon wafers by surface chemistry on silica nanobeads

Chemical experimental modeling on high surface area silica beads is explored to identify the appropriateness of the chosen precursors to lead to molecularly-precise ALD/MLD cycles. Selected growth steps of the proposed ALD/MLD process (see **scheme 1**) were carried out on silica nanobeads as a substrate (loose powder, 200 m^2/g), following an experimental molecular modeling strategy outlined elsewhere.[25]

Silica was treated at 700 °C under dynamic vacuum before ALD/MLD cycles (see SI for further details on the silica beads pre-treatment procedure). Between each half-cycle (that is a reactant pulse followed by the purge step), modified silica beds were sampled and stored separately in an argon-filled glovebox for elemental analyses, to determine chemical composition, and for spectroscopic analyses by infrared and solid-state Nuclear Magnetic Resonance (NMR).

TDMAT pulses: The TDMAT pulses were performed by connecting the TDMAT-containing bulb to the glass-tube containing the silica-based powder substrate under static vacuum (typically 10^{-5} Torr). The glass-tube under vapor pressure of TMDAT was then closed and placed in an oven at 70 °C for 4.5 hours. The glass-reactor was shaken every 30 minutes to facilitate the homogeneous exposure of the silica beads to the vapor. During the first pulse, the white silica-beads turned pale yellow.

EDT pulses: The EDT-containing flask was connected to the glass-tube containing the substrate under static Ultra-High Vacuum (UHV) at room temperature. After closure of the valve, the glass-tube was left under vapor pressure of EDT for 20 minutes at room temperature. For the first cycle, upon reaction with EDT, the powder gradually changed color from yellow to red. The glass-reactor was shaken every 5-10 minutes to homogenize the powder.

Purge steps: The purge steps were carried out to remove excess precursor vapors and by-products from the substrate after each TDMAT or EDT pulse. The steps were performed by placing the glass-tube under dynamic UHV for 30 minutes while heated in a tubular oven at 70 °C.

Analysis of the volatile by-products. At the end of each pulse and before the purge step, the volatiles were condensed in an NMR tube containing D_2O and MeOH (as internal standard).

2.3. ALD/MLD on silica-terminated silicon wafers and thermal annealing conditions

ALD/MLD experiments were performed on a 100 nm-thick thermally grown amorphous SiO_2 layer on Si wafers (herafter denoted 100 nm-SiO_2). Prior to deposition, the substrate surface was pre-treated at 200 °C in a 100 sccm of N_2 flow for 30 minutes. The sample holder temperature was 50°C during the ALD/MLD growth. The pre-treated substrate was sequentially exposed to TDMAT. TDMAT was carried by a 50 sccm flow of Ar gas. TDMAT/Ar bubbler was maintained at room temperature (25 °C). EDT evaporator was heated at 40 °C to maintain enough pressure value (P_{EDT} = 12 mbar at the beginning of the injection). Both precursors were sequentially injected into a closed reactor chamber. Between each precursor pulse, the reactor chamber was purged out with a 100 sccm flow of N_2 to remove reaction by-products.

ALD/MLD growths of 40 or 80 cycles were followed by thermal annealing at 450 °C for 30 min under 100 sccm flow of H_2(4%)/Ar(96%)with a ramp rate equal to 10 °C/min when increasing or decreasing the temperature.

2.3.1. *In situ* characterization

The two-step process on silica wafers -ALD/MLD followed by thermal annealing -, was developed in a custom-built portable reactor which mounts onto the 6-axis tower of the Newport™ diffractometer installed at the beamline SIRIUS[39] of SOLEIL synchrotron facility (see **Figure 1**). The set-up allows to use a complementary suite

of *in situ* synchrotron x-ray techniques (reflectivity, grazing-incidence fluorescence, diffraction, and absorption).[40] The SIRIUS beamline[39] has unique characteristics to work in the tender x-ray range [1.2-5] keV, such as a variable-polarization HU36 undulator source and two monochromators. Experiments with the synchrotron radiation were carried out with the direct Drive double Crystal Monochromator (DCM), which allows both step and continuous energy scanning modes with high energy resolution.

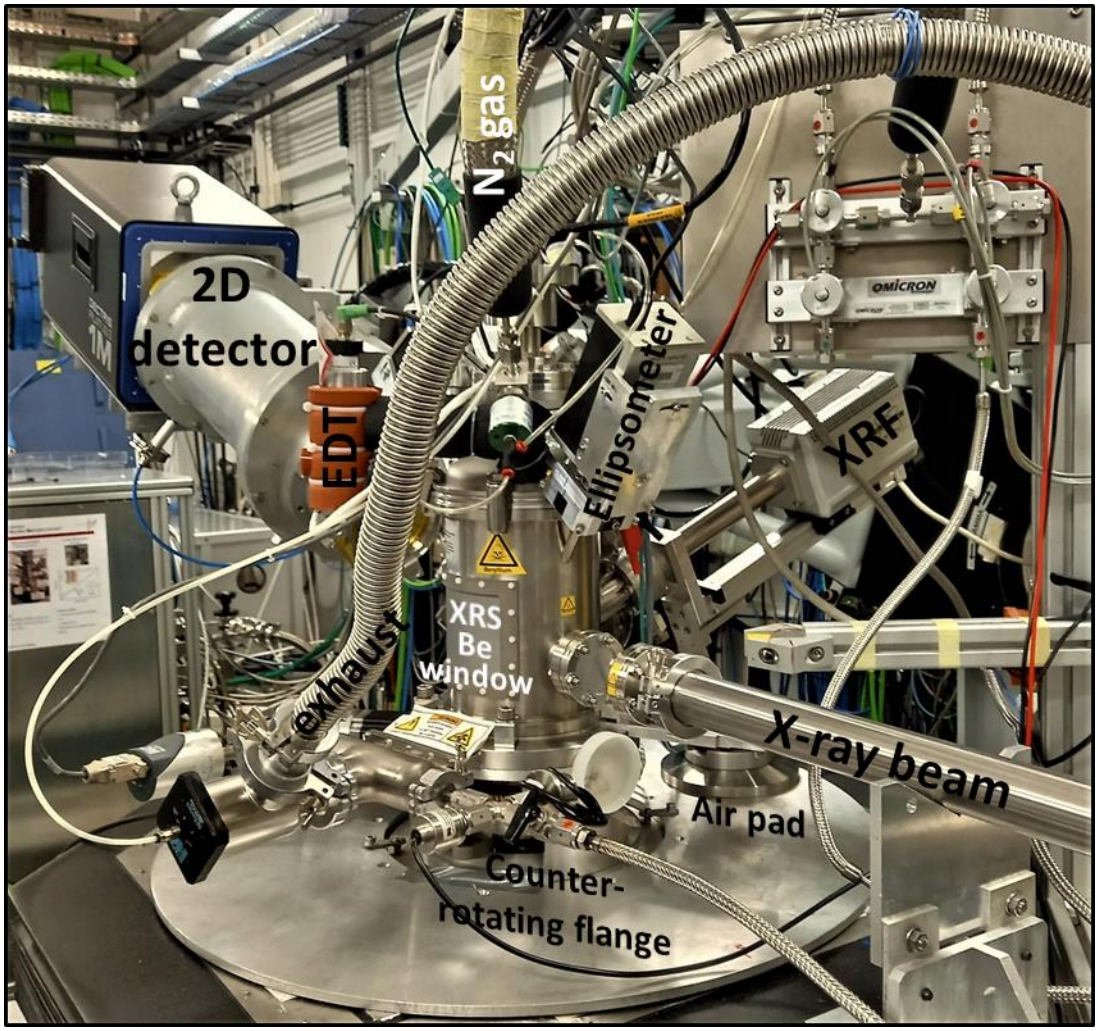

Figure 1: *ALD/MLD reactor built for surface sensitive (grazing incidence) in situ synchrotron x-ray studies, installed on the tower of the diffractometer of SIRIUS beamline (SOLEIL synchrotron).*

As shown, the reactor has x-ray transparent windows for x-ray scattering (cylindrical 400 μm thick beryllium window) and spectroscopy (20 μm thick Kapton foil) with the sample in horizontal scattering geometry. The chamber maintains several ports for ALD gas injection, fluorescence and optical measurements (ellipsometry).

Synchrotron radiation XRF and XRR have been performed *in situ* during the sample growth and subsequent thermal annealing. A four-element Silicon Drift Detector (SDD) manufactured by Bruker (XFlash QUAD 5040) was used to measure the XRF and a 2D hybrid pixel detector (PILATUS 1M by Dectris) was used to measure the XRR (and, incidentally, the x-ray scattering). The SDD was mounted on a dedicated flange of the reactor which allows to optimize the sample-detector distance; the detector nose (located into the reactor chamber) was equipped with a collimator directed at the center of the sample surface and a 20 micron-thick Kapton entrance window which separates the SDD from the chemicals in the reactor. The four-element SDD was coupled to a four-channel xMAP DXP electronics provided by XIA. For *in situ* reflected beam intensity measurement, the x-ray beam energy was equal to 5 keV and the incident angle α_i was equal to 1.2°, that is above the critical angle α_c for Si (α_c=0.35° at 5 keV). For monitoring the Ti and S XRF yields, the incoming x-ray beam energy was equal to 5 keV, i.e. above the Ti and S K-edges (4966 and 2472 eV respectively).

ALD/MLD was monitored by *in situ* multi-wavelength ellipsometry (MWE), using a 4-wavelengths (465 nm, 525 nm, 580 nm, and 635 nm) Film Sense FS-1™ Banded Wavelength Ellipsometer and FS-1 software for thickness calculation. The refractive index as a function of wavelength of the Ti-thiolate could not be measured *ex situ*, therefore we used the ellipsometry model for the calculation of TiO_2 film thicknesses.[41] Although the fit gave reasonable values during ALD/MLD, the latter

are not taken as definite in the present paper. The actual thicknesses were measured by x-ray Reflectivity (XRR).

In situ x-ray Absorption Near-Edge structure Spectroscopy (XANES) at both the Ti and S K-edges was performed in fluorescence detection mode using the four-element SDD described above. The incident angle was 1.2°. All XANES experiments were performed using a DCM monochromator equipped with Si (111) crystals, and changing the beamline HU36 undulator gap simultaneously with the monochromator Bragg angle during the continuous energy scan. A continuous energy scanning mode was used, synchronizing the speed of monochromator and undulator movements; this minimizes the acquisition deadtime and take spectra in a faster way. For Ti K-edge XANES, a couple of Pt-coated mirrors were used in order to reject high-order harmonics and focus the beam in vertical, while C-coated mirrors were used for S K-edge XANES. Grazing incidence geometry was used for all scans to limit the x-ray penetration in the substrate.

2.3.2. Ex situ characterization

XANES at the Ti K-edge were carried out after transferring the samples inside SIRIUS High Vacuum (HV) diffractometer by means of a glove box.[42] XANES spectra were recorded by scanning the incoming energy step-by-step and measuring the sample fluorescence with the four-element Silicon Drift Detector (SDD). The beamline optics setup was the same as described above for the *in situ* XANES at the Ti K-edge. For the Ti K-edge x-ray Linear Dichroism (XLD) spectra, selection of the linear vertical polarization was obtained by changing the phase of the HU36 undulator: this allows us to change from linear vertical to linear horizontal

polarization without changing the sample position and preserving the grazing incidence mode in all measurements.

Post-growth annealed samples have been characterized by Raman Spectroscopy using a Renishaw In-Via spectrometer, equipped with a Peltier cooled (CCD) detector. Raman spectra were recorded in the backscattering geometry. The light was focused onto the sample surface by a 100 x (0.85 numerical aperture) short working objective. The resulting spot diameter was around 0.7 µm. A 532 nm laser diode was used as a light source with a typical laser power of 1 mW.

Transmission electron microscopy (TEM) observations were carried out at 200 kV with a Tecnai Osiris TEM (Thermo Fisher Scientific) and equipped with a high brightness X-FEG gun and a Super-X Energy Dispersive x-ray (EDX) system comprising four detectors.

Elemental chemical components and stoichiometry were examined by XPS (x-ray Photoelectron Spectroscopy) and HAXPES (Hard x-ray Photoelectron Spectroscopy) using a PHI *Quantes* with two different monochromatized sources, either Al K_α ($h\nu$=1486.6 eV) or Chromium K_α ($h\nu$ = 5414.7 eV). The use of the novel lab-based hard x-ray sources (HAXPES) was required to investigate the oxidation of the TiS_2 layer at the surface and the in-depth distribution, this was possible thanks to the increase of the inelastic mean free path of electrons with increasing photon energy (Chromium K_α, $h\nu$ = 5414.7 eV)

Samples were prepared using a metallic clamp to ensure the electrical contact with the sample holder. Measurements using Cr source have been done at fixed angle of θ=45° and for the Al one at different angles using Angle-Resolved XPS (or ARXPS) (θ=15°, 45°, and 85°), where θ is the angle between the surface and the analyzer.

The thickness was calculated using the formula d=3 λ sin θ where λ is the photoelectron mean free path using TPP2M equation.[43] Data treatment of the measured spectra were analyzed using CasaXPS software. For spectral calibration, C 1s core peak from adventitious carbon was considered with binding energy at 284.8 eV.[38] A non-linear Shirley-type background was processed for peak fitting and the deconvolution of the peaks was obtained using the weighted least-squares calculation method of 30% Lorentzian and 70% Gaussian line shapes and Full Width at Half Maximum (FWHM) constraints.[3]

2.3.3 Four-point resistivity Measurements

Four-point probe resistivity measurements were carried out at room temperature using the Lucas-Signatone Labs Pro4 and a Keithley 2400 on 15 and 30 nm thick TiS_2/100 nm-SiO_2 thin films synthesized from 40 and 80 ALD/MLD cycles and annealing in Ar(96%)/H_2(4%) for 30 min at 450°C. Five acquisitions were performed on different spots of the film surface and substrate to check the homogeneity and calculate an average of the resistivity. The mean resistivity was obtained by multiplying the sheet resistance value ($\Omega.sq^{-1}$) by the thickness of the deposited layer. The resistivity value of the bare 100 nm-SiO_2 on silicon was too high to be measured with the equipement.[44]

2.3.4. Spectroscopic Ellipsometry

Spectroscopic ellipsometry (SE)[45] measurements were performed using two Woollam ellipsometers (RC2 in the 210-2500 nm wavelength range and IR-VASE in the mid-infrared range). The complex refractive indexes of 15 and 30 nm thick

TiS_2/100 nm-SiO_2 thin films obtained from 80 ALD/MLD cycles and annealed in Ar(96%)/H_2(4%) for 30 min, was derived from the ellipsometric measurement using a sum of 9 Gaussian oscillators. The complex refractive index was described as $N = n + ik$, where n and k are the real and imaginary part of N. The imaginary part is related to the absorption coefficient α by the formula $\alpha = 4\pi k/\lambda$, where λ is the wavelength. The bandgap of the samples were calculated using the Tauc-Plot[46] which is a representation of the function $(\alpha h\nu)^n$ versus the photon energy ($h\nu$, where h is the Planck constant).

3. Results

3.1. Molecular study of ALD/MLD process on silica beads substrate

3.1.1 Chemical reactions between the two molecular precursors in absence of substrate

Exposure of TDMAT to EDT leads to the immediate formation of an orange precipitate in pentane, while each molecule separately is soluble in pentane at the given concentrations with no formation of solid. The formation of the orange precipitate shows the existence of a thermodynamically favorable and kinetically facile pathway reaction between the two precursors. The analysis of the orange precipitate by solid-state ^{13}C NMR (see **Fig. S1**) displayed resonances compatible with the presence of organic moieties originating from EDT residues. The solid displays a weak Electron Paramagnetic Resonance (EPR) signal at g=1.98 (see **Fig. S2**), assigned to titanium(III) centers.[47]

3.1.2 Successive reactions at the gas-solid interphase between the two molecular precursors and silica beads surface

Further insight in the ALD/MLD steps of the process was obtained by reacting the precursors with silica beads, a pertinent model for studying the reaction occurring at the gas /solid interphase between precursors and substrates such as silicon-covered wafers.[25] The modeling hereafter describes the evolution during the second ALD/MLD cycle as well as during the sixth ALD/MLD cycle to show the repeatability of the surface chemistry (see **Scheme 1**).

3.1.2.1. Metal pulses on silica beads.

The *in situ* infrared (IR) spectra of solids **1**, **2**, and **3** (that is at the beginning, during, and at the end of the second ALD/MLD cycle, see **scheme 1**) are presented in **Figure 2**. The most relevant feature of the IR spectrum of sample **1** in the context of the ALD/MLD mechanism studied here is the presence of a band at 2412 cm^{-1} assigned to ν(S-H). The broad band between 2600 and 3200 cm^{-1} is assigned to hydrogen-bonded thiol moieties. Signals around 2700-3000 cm^{-1} correspond to C-H stretching vibrations arising from organic ligands. After the metal pulse, the spectrum of the resulting solid **2** showed an increase of the IR absorption band between 2700 and 3000 cm^{-1} (see blue Diffuse Reflectance Infrared Fourier Transform (DRIFT) spectrum, curve 2 in **Figure 2**), together with the reduction of the broad S-H stretching signals. Similar though shallower changes can be observed in spectra of **9** and **10** (see SI **Fig. S3**). Indeed, the analytic changes from one early cycle to the next are expected to be sharper than from a later cycle to the next, even if the surface chemistry remains similar, given the larger relative change that one single pulse is expected to bring to an early deposit than to a later one. Furthermore, in agreement with the other analytic data presented below, and as lengthily discussed in the next section (see § 4.1.3), the metal coverage is less efficient in the later cycles, leaving more unreacted thiols after the metal pulse thus explaining the large feature at 2412 cm^{-1} assigned to S-H, in spectrum **10** (**Fig. S3**) with respect to its almost complete absence in spectrum **2** (**Figure 2**).

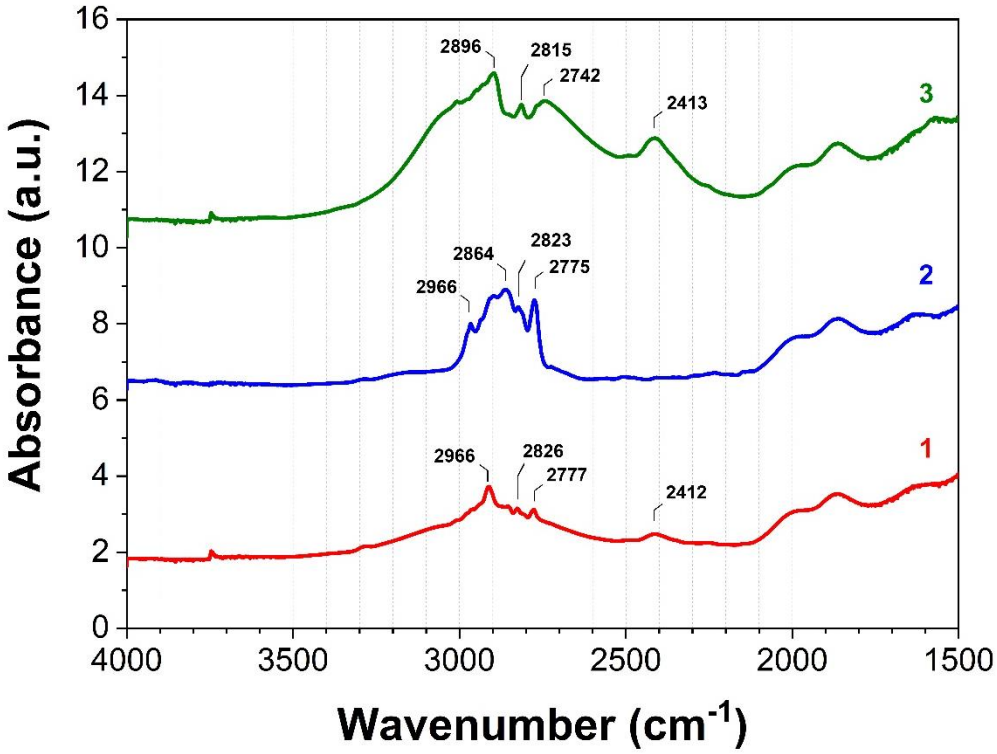

Figure 2: *IR absorbance spectra recorded during the second ALD/MLD cycle on silica nanobeads $SiO_{2\text{-}700}$ (spectrum of **1**, red); after the ALD pulse of TDMAT (spectrum **2**, blue); after the subsequent MLD pulse of EDT (spectrum **3**, green), see **Scheme 1** for numbering.*

The chemical composition of solids was determined by elemental analysis (see **Table 1**). The elemental analyses of the solids resulting from the metal pulses of the 2nd and 6th ALD/MLD cycles, *i.e.* **2** and **10**, show substantial increase in the metal content, indicating a successful metal grafting in both cases.

Table 1: *Results of elemental analyses (expressed in weight percent, $\%_{wt}$) of the solids obtained during the 2nd and 6th ALD/MLD cycles using TDMAT and EDT alternating pulse on $SiO_{2\text{-}700}$ nanobeads. See **Scheme 1** for numbering scheme.*

	Elemental analysis (wt%)					Atomic ratios		
	Ti	C	N	S	H	C/Ti	N/Ti	S/Ti
1	1.7	2.2	0.9	2.6	0.5	5.3	1.9	2.3
2	3.0	3.9	1.8	2.8	0.9	5.3	2.0	1.4
3	2.8	5.15	1.3	7.7	1.1	7.2	1.5	4.1
…								
9	4.9	9.8	2.2	15.8	2.2	8.0	1.5	4.8
10	5.5	10.3	2.4	16.1	2.3	7.4	1.5	4.3
11	5.3	10.8	2.3	17.8	2.4	8.1	1.5	5.0

During the 2nd metal pulse, the volatiles released upon TDMAT addition to **1** were collected and analysed. Dimethyl amine was observed as the sole volatile by-product of the reaction (see ^{1}H NMR study of the condensed volatile by-products in **Fig. S4**), corroborating the successful reaction of the amido precursor TDMAT at the gas-solid interphase of the growing thiolate layer.

3.1.2.2. EDT pulses on silica beads.

The sulphur pulse has been modelled by analysing the addition of EDT to the metal-terminated silica beads, **2** and **10**, followed by a purging step, leading to solids **3** and **11,** that is during the second halves of the second and sixth cycle, respectively (see **Scheme 1**).

The DRIFT spectrum for **3** (**Figure 2**, green line) exhibits a characteristic S–H bond stretching (2413 cm^{-1}) which had all but disappeared in the spectrum of **2** (**Figure 2**, blue line) and broadening of the bands between 2700 and 3000 cm^{-1}, which indicates a successful chemisorption of the thiol. ^{1}H NMR analysis of the trapped volatile by-products displayed a typical resonance corresponding to methyl protons of $HNMe_2$ (see **Fig. S5**). The changes in elemental analysis are reported in **Table 1**. The sulphur-containing solids are also EPR active (see **Fig. S2**).

3.2. ALD/MLD growth followed by annealing crystallization process on silica-terminated silicon wafers and monitoring with operando x-ray studies

The ALD/MLD growth process is based on alternating additions of TDMAT and EDT pulses to the wafer, followed by a subsequent thermal annealing of the ALD/MLD grown layer inside a dedicated reactor. This reactor, permits to control a full understanding of the atomistic mechanisms during process, as it was observed by previous work done in our research group. [40,48–52]

3.2.1 ALD/MLD growth by alternate TDMAT and EDT pulses

3.2.1.1. In situ monitoring of titanium thiolate MLD growth by MWE and XRR

Figure 3(a) shows thickness evolution during 40 growth cycles recorded by *in situ* ellipsometry and fitted using a TiO_2/100 nm-SiO_2/Si thin film model[41]. Though such a crude model prevents a quantitative analysis of the data, the thin film final thickness value measured by *in situ* XRR (13.3 nm) is compatible with the one estimated by MWE (18.2 nm). Besides, the ellipsometry data allow to ensure that

the process is robust and reproducible under SOLEIL x-ray experimental conditions. The periodic changes and saturation of the signal during the purge testify to self-limiting alternating surface reactions that insures an ALD/MLD process, as highlighted by the inset of **Figure 3(a)** showing the as-calculated total film thickness increase during a single full cycle.

Monitoring the reflected x-ray intensity provides more quantitative insights on the growth. Provided that the film roughness is not too high, the specular reflected beam intensity recorded during the deposition, at a fixed incident angle, oscillates as a function of cycle number (time) due to the film thickness evolution. A maximum (resp. minimum) of intensity corresponds to constructive (resp. destructive) interference of the beams reflected at the growing film surface and at the film/SiO_2 interface. Then, knowing the thickness oscillation period in the steady growth regime, it is possible to relate the increase of intensity inside one half an oscillation period to the film thickness increase. **Figure 3(b)** shows the increase in film thickness with the number of cycles in the range [11-17].

3.2.1.2. In situ monitoring of titanium thiolate ALD/MLD growth by XRF

Element-specific *in situ* analyses during the growth were obtained by monitoring Ti and S X-ray Fluorescence (XRF) during each successive ALD and MLD step, respectively, to quantify the Ti and S amount deposited on the sample surface. **Figure 3 (c,d)** shows Ti and S K_α fluorescence intensities normalized to the incoming x-ray beam intensity, respectively, as a function of ALD/MLD cycle number. The filled circles correspond to the fluorescence mean intensity at the end of each cycle (that is after the EDT purge). Overall, each fluorescence appears to increase linearly

after a short transient regime of growth (see linear regression fits calculated over the last 15 cycles, in the steady linear regime of growth).

The inset of **Figure 3(c)** and **Figure 3(d)** show the XRF intensity variation during the 30th to 34th cycle, representative of cycles in the steady state regime of growth, giving an insight in chemical reactions occurring at the gas-solid interphase during each pulse in the steady state. In both cases, an overall fluorescence increase is observed suggesting a successful grafting at each pulses. Some differences are also visible between the TDMAT and the EDT pulse. As for the Ti fluorescence, an initial decrease of intensity during the injection of TDMAT is observed. This drop in intensity is assigned to the presence of the TDMAT carrier gas (Ar), which leads to a significant absorption of the Ti Kα XRF because the Ti Kα energy (4509 eV) is a bit larger than the Ar K edge (3206 keV) ; upon removal of argon through the nitrogen purge the effective increase in titanium fluorescence is observed, confirming titanium enrichment of the ALD growing phase. No change in Ti fluorescence is observed after the EDT pulse, as expected since no change in titanium content is expected in the second half pulse of each cycle. As for the S fluorescence, the aforementioned drop in intensity due to the presence of argon is also observed during the TDMAT pulse but the net effect after the nitrogen pulse is null on the S fluorescence as expected. In this case, the net fluorescence increase is observed only after the EDT half-cycle. Noteworthy, the spikes of XRF intensities at the S edge, notably at low cycle number, evidence the desorption of S-containing molecules, including EDT, from the surface, suggesting that physisorbed and chemisorbed EDT are present after the EDT purge and the physisorbed excess EDT (and possibly other gaseous by-products), can be correctly removed by the nitrogen purge step. To sum

up, the XRF data shown in **Figure 3 (c,d),** also evidence a well-behaved self-limiting alternating deposition by ALD/MLD of a titanium-containing thiolate layer.

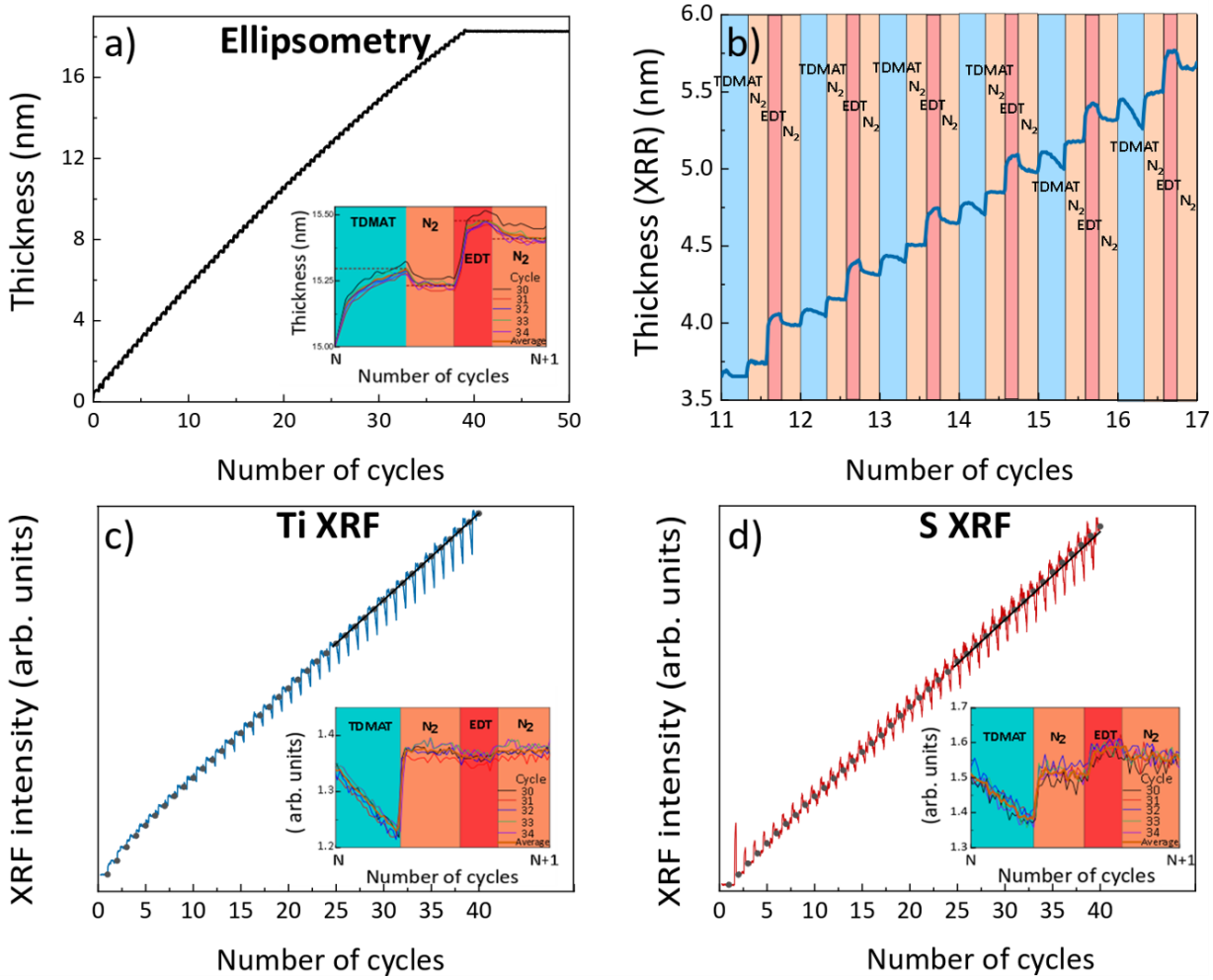

Figure 3: *Film thickness evolution measured by (a) multiwavelength ellipsometry (b) XRR at fixed angle. Ti K_α XRF intensity (blue line, c) and S K_α XRF intensity (red line, d); in both cases, the mean intensity value at the end of the EDT purge is shown for each cycle (closed black circles) together with the regression line calculated in the linear steady state regime of growth (black lines, R^2= 0.998 and 0.992, respectively). All data were recorded in situ as function of the number of cycles during the Ti-thiolate deposition ($T_{substrate}$ = 50 °C). The insets in (a), (c) and (d) show the raw data obtained during cycle numbers 30, 31, 32, 33 and 34, the curves were rescaled to be superposed.*

3.2.1.3. X-ray Absorption Near Edge Structure (XANES) of Ti-thiolate sample grown by ALD/MLD

The XANES spectra recorded at the Ti K-edge of the as-deposited Ti-thiolate thin film is reported in **Figure 4(a)**. The incoming x-ray beam linear polarization was set parallel to the growth surface. Its pre-edge peak position is at slightly lower in energy (ΔE=1 eV), with respect to the pre-edge peak position of the XANES spectra of the annealed samples (**Figure 4 (b,c,d)**); these overlap with the pre-edge peak position in the XANES spectrum of the reference TiS_2 powder, **Figure 4(e)**. The latter is a spectrum averaged over the beam polarization orientation with respect to the hexagonal crystallographic frame of the lamellar 1T-TiS_2 structure because the sample is a powder. The higher energy pre-edge peak, observed in the energy range [4972-4973] eV (A1 feature in **Figure 4**) , is well understood with regard to the 1T-TiS_2 structure.[53]. While the detailed analyses of the XANES data are beyond the scope of this paper, the energy difference between the feature of the as deposited thiolate sample (**Figure 4a**) and the one of TiS_2 (**Figure 4e**) corroborates the presence of the Ti(III) centers in the as-deposited material, as anticipated by the modeling studies reported above.

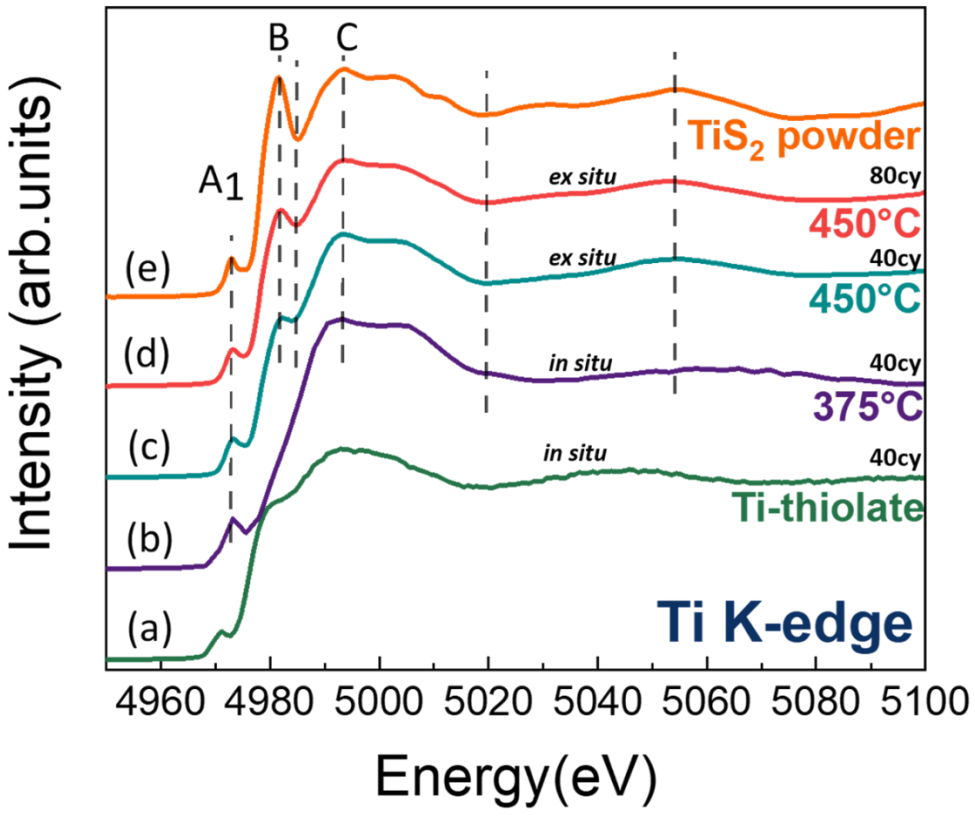

Figure 4: *In situ XANES spectra at the Ti K-edge of (a) as-deposited Ti-thiolate sample obtained after 40 cycles of ALD/MLD growth and (b) after annealing under H_2(4%)/Ar(96%) gas at 375°C for 30 minutes. Ex situ XANES spectra of Ti-thiolate samples, obtained after (c) 40 cycles and (d) 80 cycles of ALD/MLD growth and annealing at 450°C for 30minutes ; (e) ex situ XANES spectrum of a reference TiS_2 powder recorded in fluorescence mode. The linear polarization of the x-ray beam was parallel to the growth surface.*

3.2.2 Characterization of TiS_2 nano domains obtained by annealing the Ti-thiolate grown by ALD/MLD

Two Ti-thiolate samples obtained by 40 and 80 ALD/MLD cycles, respectively, were annealed at 450 °C for 30 min under H_2(4%)/Ar(96%) gas, H_2 being known to facilitate sulphur extrusion from sulphur-rich TiS_{2+x} phases.[54] The resulting phases were examined by XANES, Raman scattering spectroscopy, TEM, X-ray absorption

linear dichroism, and HAXPES to study their composition, crystallinity, and microstructure.

3.2.2.1 X-ray Absorption Near Edge Structure (XANES) of the TiS_2 samples obtained by annealing

The XANES spectra of the two annealed samples are reported in **Figure 4**(**c** and **d**, respectively). In all cases, the pre-edge peak in the energy range [4972-4973] eV (see A1 in **Figure 4**), well understood with regard to the 1T-TiS_2 structure[53], is observed. Ti^{4+} atoms in 1T-TiS_2 structure (electronic configuration: $3d^0 4s^0$) sit on a 1a position (point group -3m) of the **$P\bar{3}m1$** space group. The crystal has no inversion symmetry about this position, allowing the local hybridization of the central Ti 4p states with near neighbor Ti 3d orbitals.[53] Since Ti first nearest neighbors comprise six sulphur atoms which form a centrosymmetric octahedron, the A1 feature intensity is ascribed mainly to the dipole transition from Ti 1s to 4p character of the 3d band. Peaks B and C arise from transitions to final Ti 4p states.

Noteworthy, the pre-edge peak energy positions for all annealed samples and TiS_2 powder are the same, indicating the same formal valence of the central Ti atom (Ti^{4+}), unlike the slightly lower energy (1 eV) shifted pre-edge peak position of the sample before annealing (see **Figure 4(a)**), indicating the full conversion of the Ti(III) centers present in the as-deposited material to the expected Ti(IV) state present in TiS_2. As shown by comparing **Figure 4(c,d)**, the 80-cycles sample displays significantly improved atomic local order after annealing, with respect to the 40-cycle sample after annealing, with the local density of states tending to the one of TiS_2. Such a result could indicate that the range of atomic local order and texture reached during the annealing improve upon film thickness and the relative amount

of Ti atoms in oxidized regions at the sample surface and sulfide/SiO_2 interface is smaller in the case of the 80-cycles thin film (in agreement with TEM evidence below).

XANES spectra was also recorded *in situ* during the annealing of the sample obtained after 40 MLD cycles. **Figure 4(b)** shows the Ti K-edge XANES spectra after annealing at 375 °C for 30 min under H_2(4%)/Ar(96%) gas. The quantitative analysis of the spectra before and after annealing (**Figure 4(a)** and **(b)**, respectively) **is** out of the scope of this article. After annealing at 375 °C the spectrum shows some substantial similarities to the TiS_2 powder spectrum, firstly the increase of the distinctive pre-edge features of TiS_2. At the same time, it is clear that the TiS_2 atomic arrangement is not yet achieved and is much poorer than the one observed by annealing at 450 °C (see **Figure 4(c,d)**). Therefore, the annealing temperature increase to 450 °C seem to significantly improve the atomic local order which tends to the one of TiS_2, as the TEM results shown hereafter will also show.

3.2.2.2 Raman scattering spectroscopy

Among the fundamental active modes in Raman spectroscopy, two modes are associated to 1T-TiS_2 (space group $P\bar{3}m1$): the Eg mode (≈ 234 cm^{-1}) and A1g mode (≈ 336 cm^{-1}), corresponding to vibrations of the sulphur atoms in and out of the S-Ti-S layer, respectively. An additional shoulder mode (termed Sh-shoulder or Sh herein, ≈ 372cm^{-1}) appears more pronounced for S-Ti-S multilayer than monolayer structure.[32,55–60] The appearance of the Sh-shoulder mode is due to an excess of metal atoms between the TiS_2 layers (in the van der Waals gaps) resulting in local stiffness of the phonons.[32]

The Raman scattering spectra of the two annealed samples obtained after 40 and 80 cycles, respectively, were measured with an excitation frequency in the visible range (532 nm), **Figure 5(a,b).** The two spectra display the Eg and A1g active modes corresponding to 1T-TiS_2. The shoulder mode (Sh) is visible at about 380 cm^{-1}. By comparison with the results found in the literature and obtained with a reference TiS_2 powder, the spectra indicate a good crystalline quality of the samples with likely some defects in between the layers as corroborated by the presence of the Sh mode.[32,38]

The frequency difference between A1g and Eg modes is correlated to the average number of stacked TiS_2 layers. However, the determination of the frequency difference with precision remains difficult due to a significant asymmetry[32] of the Eg mode intensity profile (see **Figure 5(a,b)**). For this reason, the A1g mode and the better-defined Sh-shoulder mode should be preferred for the determination of the number of layers. Indeed, it has been observed in the literature that the shoulder mode (Sh) appears being more pronounced for multilayers than for a monolayer. The ratio of the integrated intensity profiles of the A1g and Sh-shoulder (A1g/Sh) can then be used for the determination of the number of TiS_2 layers (up to 5).[32,55] The obtained values show the presence of multilayers with more than 5 layers for both samples, in line with TEM images (see **Figure 5(c,d)**). By normalizing the spectra of both samples to the T2g Si peak, the integrated intensity of the A1g peak of the 40-cycle sample is half of the one of the 80-cycle sample, in agreement with the film thickness ratio (see **Fig. S6**).

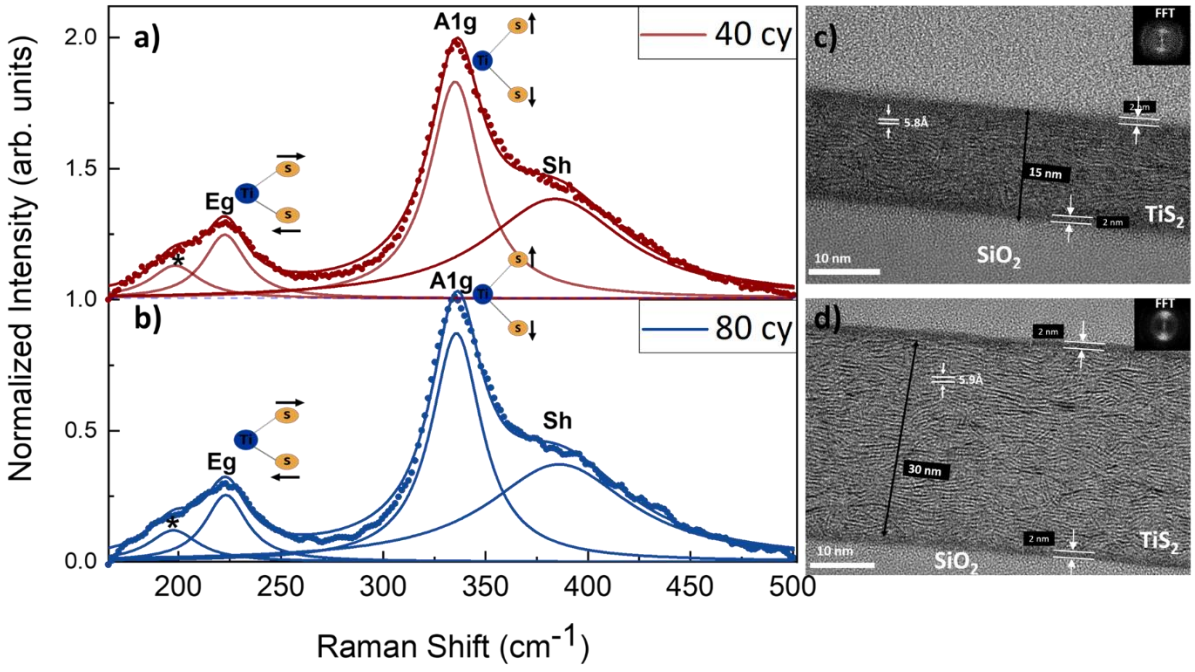

Figure 5: *(a, b) Raman spectra (dotted lines) and (c, d) cross-section TEM images of samples resulting from (a, c) 40 and (b, d) 80 ALD/MLD cycles and an annealing at 450 °C for 30 min under H_2(4%)/Ar(96%) gas. The insets in the TEM images represent the fast Fourier transform of the sample image. Raman spectra were normalized to the intensity of the A1g mode and fitted with Lorentzian curves (solid lines in a) and b) panels).*

3.2.2.3 Electron microscopy.

TEM images of the two annealed samples reveal continuous thin films with low surface roughness (see **Figure 5 (c,d)**). The nanoscale structure of the bulk of the grown phase (that is not taking into account the 2 nm thick ultimate surface and the 2 nm thick interlayer surface with the wafer substrate, both discussed below) confirms the presence of partly ordered crystalline nanodomains of atomically thin stacks of TiS_2 layers, in agreement with the Raman data discussed above. The interlayer distances equal to 5.8±0.2 Å for the 40-cycles and 5.9±0.2 Å for the 80-cycles samples are close to the bulk 1T-TiS_2 c-parameter, 5.7 Å [61]. According to the TEM images, the thickness of the deposit is, as expected, almost double for the 80-

cycles than for the 40-cycles sample (30 nm and 15 nm, respectively). The TEM images reported in **Figure 5 (c,d)** show some more pronounced atomic short-range order in the thicker 80 cycle sample than in the 40 cycle one. Regarding the ultimate surface, for both samples, the sulfide thin film is covered by an amorphous ca. 2 nm-thick top layer, which presumably results from the hydrolysis and oxidation of the material exposed to air, and should therefore be titanium oxysulfide. At the bottom, the sulfide layer/SiO_2 interface stays rather sharp. The narrowness (ca. 2 nm thick) of such interface layer, which is expected to be an oxysulfide resulting from the first pulses of the metal precursor with the pristine ultimate surface of the siliceous substrate[25], suggests a well-defined seeding chemistry from the very first pulses of the process.

3.2.2.4 Hard x-ray Photoelectron Spectroscopy (HAXPES) of annealed samples

In order to perform in-depth study of both the stoichiometry and chemical elemental components of the 30 nm thick TiS_2 thin film obtained with 80 ALD/MLD cycles and annealed at 450 °C, HAXPES was carried out using chromium K_α x-ray sources.

The analytical information depth using Cr K_α source (hv = 5414.7 eV) is about three times deeper than with the Al K_α source. The benefit of a larger sampling depth opens opportunities to minimize the contribution of the upper surface of the sample, possibly altered by the atmosphere, in the overall spectra, TiS_2 being known to convert to TiO_x by exposure to air.[62] The presence of adventitious air oxidation and hydrolysis of the top thin film (see **Figure 5(d)**), is demonstrated in a qualitative way by comparing the **Ti 1s** core level spectra to the **Ti-2p** core level spectra

presented in **Figure 6**. The mean free path of the photoelectrons calculated using TPP2M equation,[43] is found to be larger for the Ti 2p (8.1 nm) than that of the Ti 1s (1.6 nm). It follows that the analyzed thickness is about 3.3 nm with the Ti-1s core level peak instead of 15.7 nm with the Ti-2p and S-2p peaks.

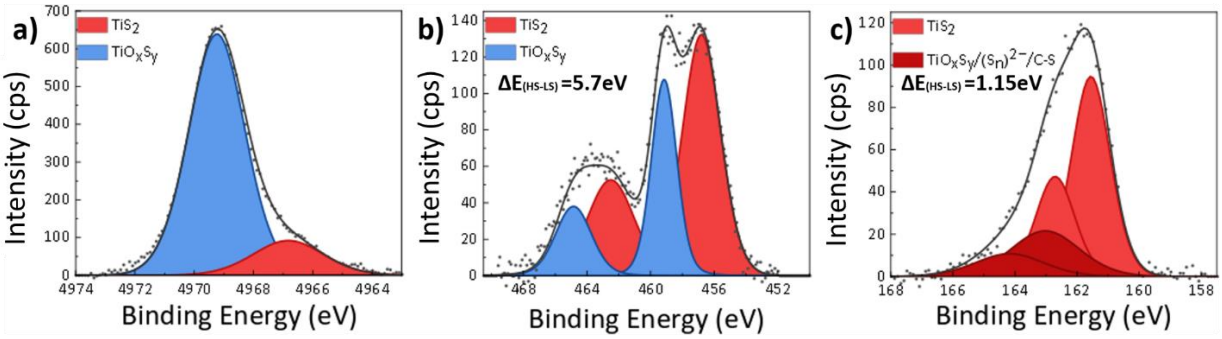

Figure 6: *HAXPES spectra measured with the Cr K_α source: Intensity as a function of the electron binding energy a) Ti-1s core peaks b) Ti-2p core peaks (doublets) and (c) S-2p core peaks (doublets).*

The Ti-1s XPS spectra shown in **Figure 6(a)** present two different environments**:** the strong signal at 4969.3 eV (84.7%, blue peak) is attributed to titanium oxysulfides whereas the weak one at 4966.8 eV (15.3 %, red peak) is attributed to TiS_2 layers. For the signal at 4969.3 eV, the thickness of the oxide layer on the top of the deposited TiS_2 layer is about 2.1 nm. The latter is in agreement with the value found by ARXPS with an Al source (see **Fig. S7**).[63] Interestingly, the oxidation of the top layer of the sample was also checked by monoatomic Ar ions etching and in-depth oxygen profiling, attesting to the absence of oxygen contamination inside the thin film (see oxygen profile **Fig. S8** in SI).

The Ti 2p XPS spectra shown in **Figure 6(b)** present two different **Ti $2p_{3/2}$:$2p_{1/2}$** spin-orbit doublets. The most intense (456.8 eV and 462.5 eV) corresponds to TiS_2.[55,64,65] The other one (459.2 eV and 464.9 eV) is assigned to the oxysulfide layer present on the top of the obtained TiS_2.[64–67] The S-2p XPS spectrum shown in **Figure**

6(c) presents also two **S $2p_{3/2}$:$2p_{½}$** components. The intense doublet (161.6 eV and 162.7 eV, spin−orbit doublet of S^{2-} species) corresponds to TiS_2.[64,67] The weak doublet signal (163.0 eV and 164.2 eV) could be attributed to the spin−orbit doublet of $(S_n)^{2-}$ species (where n=2,4,6..) known as an S-S pair and to C-S bonds. Based on the widening of the peak component presented in **Figure 6(c)** we attribute this component to a combination of $(S_2)^{2-}$ and $(S_4)^{2-}$ species.[68] It can also be referred to titanium oxysulfide environment in connection with the oxidized part already detected on the surface of the TiS_2 layer.[38,66,69,70]

Theoretical Relative Sensitivity Factors (RSF) were used to quantify the stoichiometry of the obtained TiS_2 layers.[71] The calculated aspect ratio [S]/[Ti] calculated with the Ti2p and S2p doublets attributed to TiS_2 is equal to 2.1. This indicates that the deposited film has a stoichiometry close to the one expected for TiS_2. To correlate and compare the results of HAXPES obtained with the Cr source, XPS spectra were measured with the conventional monochromatic soft Al source (Aluminum K_α, $h\nu$ = 1486.6 eV) at three different angles (θ=15°,45° and 85° with respect to the sample surface normal) for which the depth of analysis are equal to 2.3, 4.9 and 6.8 nm, respectively. The results are listed in supporting Information (see **Fig. S7**), the aspect ratio [S]/[Ti]=1.9 is in agreement with the stoichiometry obtained with the Cr source. **Table S1** shows the chemical composition proposed based on the XPS measure at the Al source and overall suggest the presence of the same environments for Ti-2p and S-2p core peaks for both the Al and Cr sources.

ARXPS data shows large amount of carbon (21%) inside the obtained layer (see **fig. S7 (i)**) which is not significantly affected by the change in take-off angle. The C 1s core level spectra exhibit three components originating from different sources. The major part corresponds to C-H/C-C bonding, it could originate from

adventitious carbon but also from the incomplete reaction of TDMAT[35] or the presence of graphitic carbon, as it was shown in a previous study regarding the synthesis of MoS_2 by the same MLD/ALD-annealing approach .[25] The presence of oxidized carbons (C-O and C=O, attributed to the as weaker contributions at 286.6 and 289.1 eV respectively, could originate from the surface contamination due to the exposure to ambient conditions[38]. Note that the line at 286.6 eV could also be assigned to C-S bonds indicating an incomplete reaction of EDT ($HSCH_2CH_2SH$).

3.2.2.5 x-ray absorption linear dichroism

The x-ray absorption linear dichroism at the Ti K-edge. **Fig. S9** in Supporting Information shows polarized Ti K-edge XANES spectra recorded with the incoming x-ray beam polarization parallel or perpendicular to the sample surface. The polarization effect in the XANES spectrum confirms the anisotropic nature of the obtained films. This was confirm at a larger scale that the e TEM images that the TiS_2 monolayers are not randomly oriented, but tend to be parallel to the substrate surface, *i.e.* the thin films show a partial texture.

3.2.2.6 Four-point probe electrical measurements and bandgap properties

Four-point probe resistivity measurements were carried out at room temperature on the 15 nm and 30 nm thick TiS_2 thin film synthesized from 40 and 80 ALD/MLD cycles and annealed in Ar(96%)/H_2(4%) for 30 min at 450°C.

The mean resistivity equal to $6.61(0.4)\times10^{-3}$ Ω.cm and $8.60(0.9)\times10^{-3}$ Ω.cm for the 15 and 30 nm thick films, respectively. The small dispersion in the values from

one spot to another attests to the homogeneity of the deposited samples. Such low mean resistivity value is in the range of values for a semi-conductor materials at room temperature. Regardless of some carbon amount in the TiS_2 thin film, a semi-conductor material has been obtained. Recently, Basuvalingam *et al.*[38] reported the growth of TiS_2 and TiS_3 layers using both thermal ALD and Plasma Enhanced-ALD from TDMAT and H_2S: Ar. Thermal ALD sample grown at 100°C lead to TiS_2 thin films with a resistivity equal to $2x10^{-3}$ Ω.cm ; PE-ALD samples grown at 150°C and 200°C lead to TiS_2 thin film with resistivity values decreasing from $9x10^{-3}$ to $3.5x10^{-3}$ Ω.cm. We can therefore conclude that our ALD/MLD process for the growth of TiS_2 thin films allows us to synthesize a material whose resistivity is in the same order of magnitude was obtained comparing to thermal ALD and PE-ALD process. Such a result could lead to use TiS_2 films as 2D contact materials with 2D semiconductors in device fabrication.

Semiconductor bandgap properties of the two samples with different thicknesses (15 and 30 nm) were investigated by spectroscopic ellipsometry (SE)[45]. **Fig. 7** shows the experimental function $(\alpha h\nu)^2$ versus $h\nu$. The n and k curves as a function of photon energy are shown in inset of **Fig. 7**. The onset of the absorption above 1 eV indicates the existence of an optical bandgap. The linear relationship between $(\alpha h\nu)^2$ and the energy at the absorption onset, is indicative of the existence of a direct band gap. By extrapolating the linear regime down to the cross point with the abscissa axis, a bandgap energy equal to 1.72 eV for the annealed sample obtained by 80 ALD/MLD cycles, a value which is very close to the one obtained with the 40 ALD/MLD cycles sample (Eg=1.74 eV). Noteworthy, a direct band gap equal to 1.70 eV was found in crystalline one-dimensional hybrid organic/inorganic TiS_2 (ethylenediamine) framework.[72]

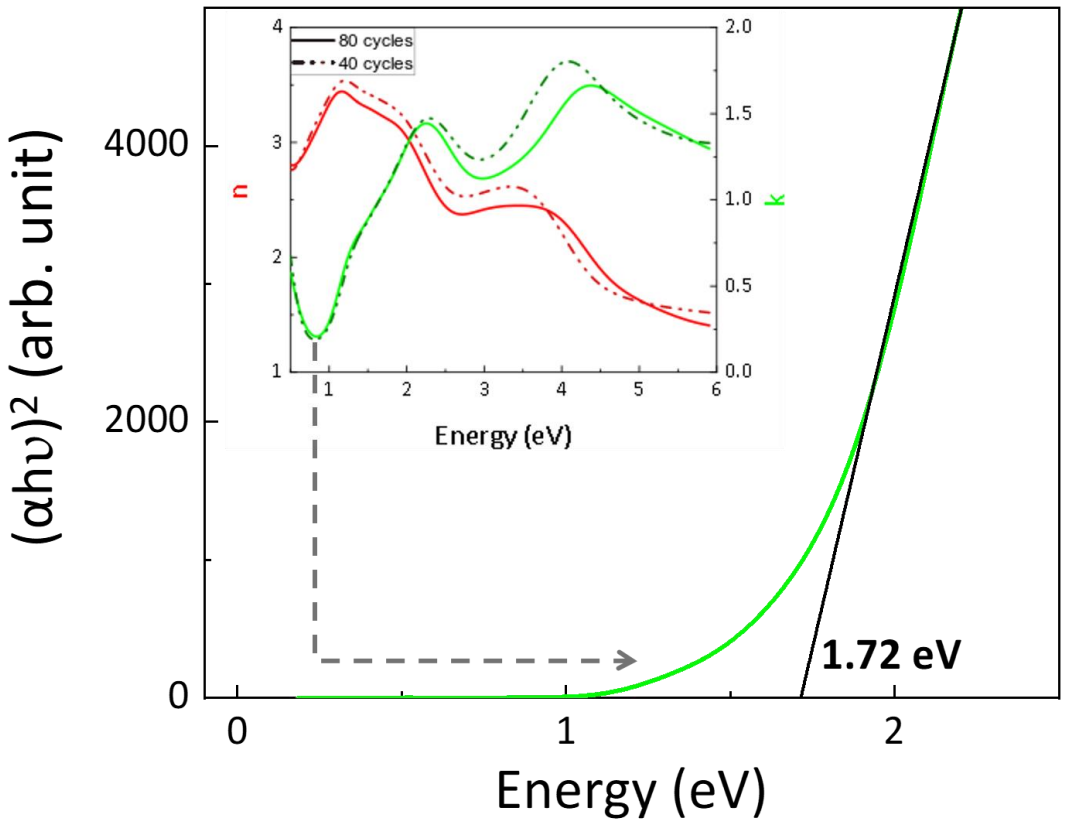

Figure 7: *Bandgap identification from the plot of $(\alpha h\nu)^2$ vs the photon energy $h\nu$, showing an estimated direct bandgap of 1.72 eV for a TiS_2/100 nm-SiO_2/Si thin film obtained from 80 ALD/MLD cycles and annealed in Ar(96%)/H2(4%) for 30 min at 450°C. The inset shows the optical constants n and k of the complex refractive index as a function of the photon energy, determined by spectroscopic ellipsometry, for thin films obtained from 40 and 80 ALD/MLD cycles and annealed in Ar(96%)/H2(4%) for 30 min at 450°C ; n and k are the real and imaginary parts, respectively.*

4. Discussion

We report a self-limiting titanium thiolate growth by Atomic Layer Deposition/Molecular Layer Deposition (ALD/MLD) on 100 nm-thick thermally-grown SiO_2 on Si at low temperature (50 °C). From it, lamellar TiS_2 thin films can be obtained by thermal annealing under H_2/Ar at a mild temperature (450 °C, with crystallization starting at even lower temperatures). Organic carbon and $(S_n)^{2-}$ presence show that the annealing is not complete. The films are continuous, smooth, homogeneous, and as thin as 15 nm or even less so. To the best of our knowledge, TiS_2 material has never been obtained with an ALD/MLD approach. The electric measurements on the 15-nm and 30-nm thick thin films show a semi-conductor behavior with direct band-gap.

Hereafter some other noteworthy aspects of the process are discussed, namely i) the growth mechanistic insight gained through the modeling studies on silica beads, ii) the growth mechanistic insight gained from *in situ* x-ray studies and comparison with the modeling studies and iii) the preferential orientation of TiS_2 despite the amorphous nature of the substrate.

4.1. Thiolate growth mechanistic insight on model silica beads

The development of ALD-grown molecularly-thin layers of MoS_2 on silica-covered silicon wafer was steered by the study of the chemical reactions between the two precursors in absence of substrate and in the presence of high surface area silica beads. [25] Herein, we successfully extended this molecular approach for studying the reaction of TDMAT and EDT, *en route* to the targeted ALD/MLD process toward TiS_2.

4.1.1 Reaction between TDMAT and EDT

First of all, the thermodynamically accessible and kinetically facile reaction of molecular precursors (TDMAT and EDT) among themselves is insightful since it tends to suggest that an MLD/ALD process targeting TiS_2 and based on their alternate addition should lead to film growth. However, because of the absence of a substrate, this reactivity results in coordination polymers which are difficult to characterize, with no special control over their molecular weight. More importantly in the context of ALD, the presence of the self-limiting nature of the reaction cannot be investigated by studying the reactivity of the molecular precursors with each other.

4.1.2 The interest of silica beads

The ALD reaction mechanism was therefore established by investigating the chemistry occurring at the surface of porous silica nanobeads, as a model for the flat wafer substrate. The analogy between the 3D surface of silica powders and 2D surfaces of silica-covered silicon wafer substrates was proposed 25 years ago.[73] The study showed that the ultimate surface of both 2D and 3D substrates are very close in terms of chemical nature of the reactive sites (silanols, SiO-H), and in terms of site density as a function of pretreatment temperature. More recently, Surface OrganoMetallic Chemistry (SOMC) studies[74] provided titration and reactivity studies which have further corroborated the validity of this analogy between pristine flat and porous substrates toward a first metal pulse.[75–77] The fact that the density of the anchoring site is proven to be comparable for the two supports tends to suggest that no different steric hindrance considerations should play for the

chemistry occurring on the surface of the silica powder versus the one occurring on the surface of the silica on the wafer. The diffusion of precursor is surely different when exposed to a flat surface with respect to a powder; at the same time, the nature of the (ideal) MLD /ALD process is to be chemistry driven (rather than diffusion controlled). Therefore, if sufficient precaution is taken to allow the equilibrium to be reached - and this means long reaction time with the powder in particular, as is the case in our work - this difference is not anticipated to be problematic. Furthermore, monitoring with IR allows to have a spectroscopic handle to gauge *in situ* the change in reaction advancement over time and hence handle possible diffusion limitations. The main differences between the two supports remains the overall number of actives sites between the types of experiments performed (performed on typical scales of hundreds of miligrams of silica powders having large specific surface area, typically, 200 $m^2.g^{-1}$, and much fewer milligrams of silica of non-porous wafer with geometric surface area of the order of 10^{-2} $m^2.g^{-1}$). It is exactly this significant order of magnitude difference in favor of the powder that allows to use spectroscopic and analytic tools on the powder inaccessible to the wafer (see below), and yet, because density is analogous and diffusion is taken care of, the powder chemistry, with its new molecular-level insight, has a chance to mimic satisfactorily the chemistry on the wafer. As mentioned above, our first attempt to use this analogy to model a full ALD process was successful for growing ultra-thin crystalline MoS_2 nanodomains from $Mo(NMe_2)_4$ and EDT .[25]

In the present case, silica-beads model studies demonstrate the successful chemisorption of both the metal and the sulphur-containing precursors which ensures mass gain upon each respective ALD or MLD pulse *en route* to TiS_2.

4.1.3 Metal pulse mechanism

The IR monitoring of the silica beads upon exposure to $Ti(NMe_2)_4$ pulses and the connected changes in elemental composition (see **Table 1**) show that titanium amido bonds in the precursor react with surface sites with concurrent amine release. This reaction appears complete for the first pulse. The IR spectrum shows a weak band at 3650 cm^{-1}, distinctive of scant residual surface silanols after the metal pulse. The titanium loading in **1** of **Scheme 1** (1.7 %w, equivalent to 1.1 Ti/nm^2 on the 200m^2/g beads used here) is also indicative of a complete coverage, based on the known concentration of the reactive sites on the starting substrate (ca. 1.15 OH /nm^2 for silica pre-treated *in vacuo* at 700 °C)[78].

In analogy with the established ALD concept of monolayer (ML, fully formed layer resulting from an ideal ALD cycle) and Growth Per Cycle (GPC, expressed phenomenologically in nm/cycle or as a fraction of ML/cycle when the ideal ALD growth mechanism is considered), we can express the chemical data herein by introducing corresponding concepts such as Chemical Maximum Coverage, CMC, and Surface Reaction Advancement per Half-Cycle, SRApHC, respectively. These concepts (CMC and SRApHC) are related yet distinct from ML and GPC since the latter are defined on the basis of the composition and density of final targeted phase (TiS_2 here) while the formers are related to the “as deposited” material (titanium thiolate here). Adopting these distinct metrics could help bridge the gap

between the recurrent hiatus between the (ideal) targeted final phase of the reality of the "as deposited" material during the ALD process.

For the first metal pulse, the combined analyses have suggested a full coverage, SRApHC (1st Ti-pulse) = 1.0 CMC. During the metal pulse of the second cycle, the elemental analysis shows an increase of the Ti weight fraction from 1.7% to 3.0% leading to an approximate atomic composition increase from (surface)-$[Ti]_1$ to (surface)-$[Ti]_{1.7}$, showing that there is a substantial yet not complete surface reaction advancement (70% with respect to the maximum possible for a simple 1:1 stoichiometric growth, *i.e.* SRApHC (2nd Ti-pulse) $\leq$ 0.7 CMC). During this second cycle, the other changes in relative molar ratios of the elements that can be calculated from the elemental analyses similarly show that there is a substantial but not full surface reaction advancement. Similarly, the empirical formula (see C/Ti, N/Ti, and S/Ti ratios evolution in **Table 1**) account for the co-existence of newly metalated surface species and unreacted thiol terminated starting species. Therefore, only part of the available reactive sites, the thiols SH groups, react with TDMAT.

During the 6th cycle, the metal content increases after the TDMAT pulse by ca. 10% (from 4.9w% to 5.5w%, see **Table 1**). To a first approximation a complete coverage during the 6th cycle can be expected to lead to a 20% increase in the value (from surface-$[Ti]_5$, to surface-$[Ti]_6$). Therefore, the titanium loading change during the metal pulse of the 6th cycle suggests that the surface reaction advancement is at best 50%, SRApHC (6nd Ti-pulse) $\leq$0.5 CMC.

Overall, these changes suggest that during the MLD/ALD step, TDMAT successfully reacts with the surface thiol groups, by replacement of a titanium amido with a

thiolate bond with concurrent amine release (see **Scheme 2** for a proposed generic average surface reaction scheme for the metal pulse). Only part of the available SH groups react with TDMAT leading the co-existence of newly metalated surface species and unreacted thiol terminated starting species, with a concurrent decrease in surface reaction advancement per half-cycle, SRApHC along the MLD process, at least up to the few cycles modelled here. **Scheme 2** reports a proposed generic average surface reaction scheme for the metal pulse, with an overall decrease in surface reaction advancement per half-cycle, SRAPHC along the MLD process.

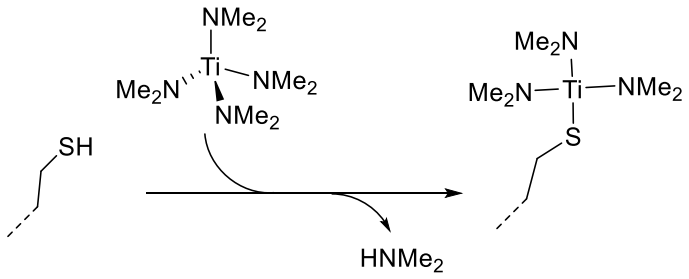

n^{th} ALD Cycle	Molar fraction of ultimate surface composition			Surface Reaction Advancement Per Half-Cycle (SRAPHC) as fraction of Chemical Maximum Coverage (CMC)
2^{nd}	1	starting amount before metal pulse (a.u)	0	< 0.7 CMC
	0.3	final amount after metal pulse (a.u)	0.7	
6^{th}	(1-n)	starting amount before metal pulse (a.u)	n	< 0.5 CMC
	(1-n)-0.5	final amount after metal pulse (a.u)	n+ 0.5	

Scheme 2*: Proposed general reaction scheme for a metal pulse. The surface reaction advancement per half-cycle, SRAPHC , expressed as fraction of the chemical maximum coverage CMC, calculated from quantitative analytic studies on silica beads models during the 2^{nd} and 6^{th} cycles are reported in the table.*

4.1.4 The thiol pulse mechanism

The IR monitoring of the silica beads, the analysis of the gas phase and the connected changes in elemental analyses suggest that EDT reacts, at least partially, with the Ti-NMe_2 amido moieties present at the surface of the support by protonolysis, leading to the formation of a Ti-SCH_2CH_2SH thiolate group concomitantly with release of $HNMe_2$ in the gas phase. This agrees with literature in molecular chemistry. [79]

Elemental analysis displayed substantial increase of the S/Ti atomic ratio (from 1.4 to 4.1 during the EDT pulse of the second cycle), indicating that on average between one and two EDT ligands (that is between 2 and 4 sulphur atoms) are added per titanium center. Concurrently, the N/Ti ratio drops but is not nul suggesting that only part of the available dimethyl-amino-based ligands is substituted by EDT. Noteworthy, the C/Ti ratio also increases (from 5.3 to 7.2, see **Table 1).** Simple substitution of $-NMe_2$ ligand by $-SCH_2CH_2SH$ ligand should not, in principle, increase the number of carbon atoms (with respect to Ti). Such an increase may point to incomplete release of $-NMe_2$ ligands. Consistently, the observed drop in nitrogen content (N/Ti) is less than the one expected based on simple amido per thiolate substitution. Protonation of the amido ligand during the protonolysis exchange reaction with the thiol and coordination of part of the resulting amine to the metal centre is an explanation consistent with these data. Proton transfer reactions between thiols and nitrogen-based moieties, $(HS\text{-}C_n\text{-}S)^- + (NMe_2)^- \rightarrow (S\text{-}C_n\text{-}S)^{2-} + (HNMe_2)$ (see structure (c) in **Scheme 3**), that has literature precedents, could also be invoked.[80,81]

The sulphur-containing solids also EPR active, like the molecular polymer resulting from mixture of EDT and TDMAT (see **Fig. S4**). The fact that the solid resulting from EDT addition are EPR active suggests that the reaction between the

EDT and TDMAT does not simply imply ligand exchange, as observed for the molybdenum (IV) analogous system,[25] and involves redox activity between the titanium(IV) precursor and the sulphur-containing ligand, as already observed in molecular chemistry for several reactions of metal amido complexes with thiols. [82] Thiol ligands are known to be reducing agents by -SH coupling.[83] While the full interpretation of these EPR signals goes beyond the scope of this paper, overall, these EPR data show the presence of redox Ti^{III}/Ti^{IV} surface reactions concomitant with thiol/amido ligand exchange reactions described above. Therefore, the surface chemistry goes beyond a simple thiol for amido substitution reaction and entails a complex set of reactions (see **Scheme 3**).

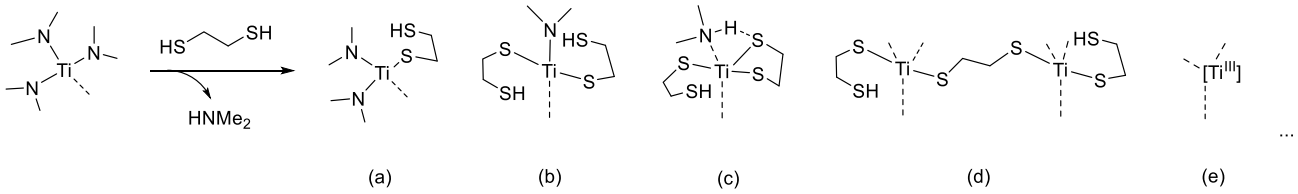

Scheme 3: *Examples of possible surface reactions occurring during the sulphur pulse of the process: (a) mono-substitution and (b) bi-substitution of titanium amido ligands by EDT by protonolysis and release of dimethylamine; concurrent partial (c) proton exchange between thiol and amido ligands; (d) bridging dithiol substitution and (e) redox reactions leading to titanium(III).*

4.1.5 Summary of The MLD mechanism on silica beads

In summary, silica-beads model studies demonstrate the successful chemisorption of both the metal and the sulphur-containing precursors by a self-limiting growth of a titanium thiolate phase upon each respective ALD or MLD pulse. The approach proposed here allows having mass gain information *on each element separately*, through elemental analyses, for example, thus offering a well-

nuanced description of the surface chemistry occurring at the interface (see **Scheme 2** and **Scheme 3**). This could be an interesting addition to other type of mechanistic studies in ALD, for example through QCM studies, which can obtain global, rather than element specific, mass gain at each half pulse to infer the molecular-level chemical reactions occurring at the gas-solid interface of the substrate.

4.2. Thiolate growth mechanistic insight through in situ x-ray studies

Informed in part by the insightful molecular studies presented above, we have successfully employed *in situ* x-ray study for assessing the quality of a new innovative two-step process to TiS_2 thin films on wafers. Both the thiolate growth and its annealing were studied inside the ALD reactor. The synchrotron brilliance enabled the study of targeted material growth, under the actual process conditions and from the first pulse. The possibility to record both the S K_α and Ti K_α fluorescence yield has allowed us to monitor the S/Ti ratio during the thiolate growth and during its annealing, the fluorescence yield being directly proportional to the amount of element deposited on the surface (in the case of ultra-thin films x-ray absorption is negligible). Over the process, this S/Ti ratio clearly increases. A similar trend is observed in the molecular studies on silica beads, which proposes the following molecular explanation: in the early cycles, while less than 1 Ti per S is added during a metal pulse (see **scheme 2**), between 1 and 2 EDT per Ti are added during the EDT pulse (**scheme 3**). Another example where directly comparable insight are accessible for the powder and wafer approaches is given by the observed partial reduction of Ti(IV) to TI(III) during the sulfur pulse in both systems. The

presence of S radical signature observed in EPR activity of the layers grown on the silica-beads correlates to the formation of dithiol moieties identified through the HAXPES and XPS studies on wafer alongside the presence of Ti(III) center proposed based on the XANES studies. These similarities corroborate a founding tenet of our work: that the two systems (powder and wafer) display very similar surface chemistry.

X-ray reflectivity data obtained *in situ*, in real time at a fixed angle of reflectivity allowed to measure the film thickness increase as a function of cycle number (see **Figure 3(b)**). Each precursor injection leads to a clear jump in thickness which reaches a constant value during each purge, corroborating the self-limiting surface chemistry observed by MWE and XRF (see **Figure 3 (a,c,d)**). During the steady growth regime, the resulting average growth per cycle (GPC) can be estimated as 0.32 $nm.cy^{-1}$. The latter value, agrees with the average GPC value obtained from *in situ* XRR curve measured by varying the incident angle (usual XRR mode), after deposition of 40-cycles thin film (0.33 $nm.cy^{-1}$, see supporting information **Fig. S10**). Also, the resolution of the *in situ* XRR at fixed angle of reflectivity during ALD/MLD study allows to determine the growth per each half-cycle: the thickness gain can be estimated as 0.18 $nm.cy^{-1}$ during TDMAT half-cycle and 0.14 $nm.cy^{-1}$ for EDT half-cycle. As in the silica beads study, the first pulses display markedly different changes in fluorescence with respect to later ones. This datum is coherent with an expected increase of the steric hindrance upon film growth (at least in the very early stages).

The two main approaches explored here, *in situ* synchrotron-based study and ALD/MLD modeling on large surface area silica beads, appear complementary and lead to sharply molecularly precise insights in the ALD/MLD process' mechanism on the wafer. Interestingly, new specific conceptual tools are thus required for this combination ("real-on wafer" and "model-on powder" ALD/MLD) to be operable, such as the concept of chemical maximum coverage (CMC) and surface reaction advancement per half cycle, SRApHC, introduced in the silica study above and to be put in echo with the concept of monolayer (ML) and Growth per cycle (GPC) in ALD.

In summary, the insightful complementarities between the two approaches comforts in pursuing such tandem approach.

4.3. Preferential TiS_2 orientation parallel to the substrate

The process has achieved nanodomains of crystalline TiS_2 behaving as semiconductor with direct band-gap with the TiS_2 layers preferentially oriented parallel to the amorphous substrate surface (SiO_2). Comparison with state-of-the-art shows that this achievement is a substantial novelty.

Thus far, the ALD growth of crystalline TiS_2 layers parallel to the substrate surface was achieved from $TiCl_4$ and H_2S precursors only on crystalline substrates such as ZnS[7] and the c-sapphire substrate surface[2], albeit several substrates were tested, such as sodalime glass, native-SiO_2/Si, ZnS, Rh, Ir, Pd, Pt, Ru, and TiN by Pore *et al*. [7], Si(100), stainless steel, c-sapphire and quartz by Sayed *et al*. [2] and Al_2O_3-coated native SiO_2 on Si(111) substrate[34], carbon paper, or germanium.[36] Amorphous TiS_2 or TiS_3 films where obtained when H_2S (at 180°C) was used in combination with the TDMAT precursor used herein. [35] TiS_2 and TiS_3 layers were

also obtained by using both thermal ALD and Plasma Enhanced-ALD from TDMAT. [38] Post-growing treatment such as rubbing which yields mechanical alignement[7] or exposure to sulphur rich atmosphere during post-annealing are worth mentioning as alternative routes to obtain some alignment crystallization. Noteworthy, the vertically aligned TiS_2 nanowall network obtained on the c-sapphire substrate surface grew on top of an amorphous TiS_2, parallel to the film-substrate interface, along with TiS_2 platelets grown away from the substrate surface.

This shows that albeit successfully orienting the TiS_2 layers, the C-sapphire also suffers from non-well-defined initial cycles and concurrent out-of-plane crystallization which mars the quality of the process, especially if ultra-thin deposits are targeted. In our case, such ill-defined interphase does not appear to be present (and is echoed by the homogeneous full-coverage observed on silica beads).

In summary, the hybrid ALD/MLD step appears to achieve complete coverage (1 CMC) of the starting support from the first pulse, based on the results obtained on the silica bead (the "model" system). We posit that this full coverage occurs also on the wafer (the "real" system) and contributes to the very thin interlayer between the support and the final TiS_2 phase observed by TEM on the wafer (see **figure 5(c,d)**), and hence contributes to the quality of the final film. The fully amorphous thiolate phase is then crystallized in a separate step. We posit that the initial lack of crystalline order is beneficial to the final preferential orientation of the TiS_2 nanodomains since it prevents the coexistence of differently oriented crystallization seeds before the bulk crystallization temperature is reached. This result consolidates the pertinence of the two-step approach -first: hybrid ALD/MLD and second: annealing- presented in the introduction.

5. Conclusion

In the quest for large-scale deposition methods of 2D TMDC materials, ALD has proven many successes but also limitations, among which the difficulty to produce films with preferential orientation parallel to the substrate, especially if amorphous. We have reported here synthesis strategy alternative to ALD, based on the combination of an ALD metal-pulse (TDMAT) with an organic-precursor MLD pulse (EDT) followed by annealing and applied it to the preparation titanium disulfide (TiS_2). Combining TDMAT and EDT in an ALD/MLD process generates a thin amorphous hybrid organic-inorganic Ti-thiolate material that can be converted into lamellar TiS_2 layers by thermal annealing under H_2(4%)/Ar(96%) at 450 °C.

Deep understanding and fine control of both steps could be achieved by *in situ* synchrotron XRF, XRD, and XAFS studies during alternating ALD and MLD pulses and annealing steps in a dedicated reactor setup, *ex situ* characterizations for the final phase (NMR, TEM, HAXPES, and Raman scattering), and chemical experimental modeling on high surface area silica beads for the initial cycles of the ALD/MLD process. For this latter study, we have proposed two actionable new parameters, related yet distinct to the established *monolayer* (ML) and *growth-per-cycle* (GPC) parameters used in ALD studies, namely the *chemical maximum coverage* (CMC), and *surface reaction advancement per half-cycle* (SRApHC), as in order to sharpen the description of the chemical reactions occurring at the gas-solid interphase in the MLD/ALD processes, and helping to achieve a performing well-behaved chemical process growth process prepared by hybrid ALD/MLD.

The usefulness of strategy followed here, that is decoupling growth from crystallization, seems well adapted to TMDC and opens new possibilities for the synthesis of 2D materials in general.

Acknowledgments

The work was financially supported by the ANR project ANR-18-CE09-0031. The Ph.D. work of P.A.Y. is financed by the Labex MINOS (ANR-10-LABX-55-01). The authors acknowledge the facilities and the scientific and technical assistance of the CMTC characterization platform of Grenoble INP supported by the Centre of Excellence of Multifunctional Architectured Materials (CEMAM) ANR-10-LABX-44-01 funded by the “Investments for the Future” Program; as well as facilities at the IRCELYON (UMR 5256 under double tutelage CNRS and Université Claude Bernard Lyon 1) and CP2M laboratories (UMR 5128, under triple tutelage CNRS, CPE Lyon, and Université Claude Bernard Lyon 1, into which the former unit C2P2 UMR 5265 where part of this work was carried out merged). The experiment at the SIRIUS beamline benefited from the SOLEIL beam time allocation no. 20190732. SIRIUS HV diffractometer was funded by the Swedish Research Council (Vetenskapsrådet MAX IV–SOLEIL collaboration) and by the Île-de-France region (project ‘FORTE’, DIM OXYMORE). A part of this work, carried out on the Platform for Nanocharacterisation (PFNC), was supported by the “Recherche Technologique de Base” program of the French National Research Agency (ANR). We also acknowledge the support of the Tandems collaboration project between PHI and Leti. We acknowledge D. De Barros for ALD reactor engineering assistance and SERMA technologies for TEM measurements.

1

References

1. Venkata Subbaiah, Y. P., Saji, K. J. & Tiwari, A. Atomically Thin MoS2 : A Versatile Nongraphene 2D Material . *Adv. Funct. Mater.* **26**, 2046–2069 (2016).
2. Sayed, F. N., Sreedhara, M. B., Soni, A., Bhat, U., Datta, R., Bhattacharyya, A. J., & Rao, C. N. R. Li and Na-ion diffusion and intercalation characteristics in vertically aligned TiS2 nanowall network grown using atomic layer deposition. *Mater. Res. Express* **6**, (2019).
3. Flamary-Mespoulie, F., Boulineau, A., Martinez, H., Suchomel, M. R., Delmas, C., Pecquenard, B., & Le Cras, F. Lithium-rich layered titanium sulfides: Cobalt- and Nickel-free high capacity cathode materials for lithium-ion batteries. *Energy Storage Mater.* **26**, 213–222 (2020).
4. Zhang, L., Sun, D., Kang, J., Wang, H. T., Hsieh, S. H., Pong, W. F., ... & Guo, J. Tracking the Chemical and Structural Evolution of the TiS2 Electrode in the Lithium-Ion Cell Using Operando X-ray Absorption Spectroscopy. *Nano Lett.* **18**, 4506–4515 (2018).
5. Keum, D. H., Cho, S., Kim, J. H., Choe, D. H., Sung, H. J., Kan, M., ... & Lee, Y. H. Bandgap opening in few-layered monoclinic MoTe2. *Nat. Phys.* **11**, 482–486 (2015).
6. Muller, G. A., Cook, J. B., Kim, H. S., Tolbert, S. H. & Dunn, B. High performance pseudocapacitor based on 2D layered metal chalcogenide nanocrystals. *Nano Lett.* **15**, 1911–1917 (2015).
7. Pore, V., Ritala, M. & Leskelä, M. Atomic layer deposition of titanium disulfide thin films. *Chem. Vap. Depos.* **13**, 163–168 (2007).
8. Harshman, D. R. & Mills, A. P. Concerning the nature of high-Tc superconductivity: Survey of experimental properties and implications for interlayer coupling. *Phys. Rev. B* **45**, 10684–10712 (1992).
9. Wan, C., Kodama, Y., Kondo, M., Sasai, R., Qian, X., Gu, X., ... & Koumoto, K. Dielectric Mismatch Mediates Carrier Mobility in Organic-Intercalated Layered TiS2. *Nano Lett.* **15**, 6302–6308 (2015).
10. Wu, X. C., Tao, Y. R. & Gao, Q. X. Preparation and field emission properties of titanium polysulfide nanobelt films. *Nano Res.* **2**, 558–564 (2009).

11. Brune, V., Grosch, M., Weißing, R., Hartl, F., Frank, M., Mishra, S., & Mathur, S. Influence of the choice of precursors on the synthesis of two-dimensional transition metal dichalcogenides. *Dalt. Trans.* **50**, 12365–12385 (2021).

12. Hao, S., Zhao, X., Cheng, Q., Xing, Y., Ma, W., Wang, X., ... & Xu, X. A Mini Review of the Preparation and Photocatalytic Properties of Two-Dimensional Materials. *Front. Chem.* **8**, 1–11 (2020).

13. George, S. M. Atomic layer deposition: An overview. *Chem. Rev.* **110**, 111–131 (2010).

14. Mattinen, M., Leskelä, M. & Ritala, M. Atomic Layer Deposition of 2D Metal Dichalcogenides for Electronics, Catalysis, Energy Storage, and Beyond. *Adv. Mater. Interfaces* **8**, 1–47 (2021).

15. Cai, J., Han, X., Wang, X. & Meng, X. Atomic Layer Deposition of Two-Dimensional Layered Materials: Processes, Growth Mechanisms, and Characteristics. *Matter* **2**, 587–630 (2020).

16. Kim, Y., Woo, W. J., Kim, D., Lee, S., Chung, S. M., Park, J., & Kim, H. Atomic-Layer-Deposition-Based 2D Transition Metal Chalcogenides: Synthesis, Modulation, and Applications. *Adv. Mater.* **33**, 1–33 (2021).

17. Park, G. H., Nielsch, K. & Thomas, A. 2D Transition Metal Dichalcogenide Thin Films Obtained by Chemical Gas Phase Deposition Techniques. *Adv. Mater. Interfaces* **6**, 1–31 (2019).

18. Zhang, H., van Pelt, T., Mehta, A. N., Bender, H., Radu, I., Caymax, M., ... & Delabie, A. Nucleation and growth mechanism of 2D SnS2 by chemical vapor deposition: Initial 3D growth followed by 2D lateral growth. *2D Mater.* **5**, (2018).

19. Multia, J. & Karppinen, M. Atomic/Molecular Layer Deposition for Designer's Functional Metal–Organic Materials. *Adv. Mater. Interfaces* 2200210 (2022).

20. Zhao, Y., Zhang, L., Liu, J., Adair, K., Zhao, F., Sun, Y., ... & Sun, X. Atomic/molecular layer deposition for energy storage and conversion. *Chem. Soc. Rev.* **50**, 3889–3956 (2021).

21. Meng, X. An overview of molecular layer deposition for organic and organic-inorganic hybrid materials: Mechanisms, growth characteristics, and promising applications. *J. Mater. Chem. A* **5**, 18326–18378 (2017).

22. Abi Younes, P., Sayegh, S., Nada, A. A., Weber, M., Iatsunskyi, I., Coy, E., ... & Bechelany, M. Elaboration of porous alumina nanofibers by electrospinning and molecular layer deposition for organic pollutant removal. *Colloids Surfaces A Physicochem. Eng. Asp.* **628**, 127274 (2021).

23. Van de Kerckhove, K., Dendooven, J. & Detavernier, C. Annealing of thin "Tincone" films, a tin-based hybrid material deposited by molecular layer deposition, in reducing, inert, and oxidizing atmospheres. *J. Vac. Sci. Technol. A* **36**, 051506 (2018).

24. Van de Kerckhove, K., Mattelaer, F., Dendooven, J. & Detavernier, C. Molecular layer deposition of "vanadicone", a vanadium-based hybrid material, as an electrode for lithium-ion batteries. *Dalt. Trans.* **46**, 4542–4553 (2017).

25. Cadot, S., Renault, O., Frégnaux, M., Rouchon, D., Nolot, E., Szeto, K., ... & Quadrelli, E. A. A novel 2-step ALD route to ultra-thin MoS2 films on SiO2 through a surface organometallic intermediate. *Nanoscale* **9**, 467–950 (2016).

26. Peters, E. S., Carmalt, C. J. & Parkin, I. P. Dual-source chemical vapour deposition of titanium sulfide thin films from tetrakisdimethylamidotitanium and sulfur precursors. *Journal of Materials Chemistry* ***14***, 3474-3477 (2004).

27. Palgrave, R. G. & Parkin, I. P. Chemical vapour deposition of titanium chalcogenides and pnictides and tungsten oxide thin films. *New Journal of Chemistry* ***30,*** 505-514 (2006).

28. Carmalt, C. J., Parkin, I. P. & Peters, E. S. Atmospheric pressure chemical vapour deposition of TiS2 thin films on glass. *Polyhedron* **22**, 1263–1269 (2003).

29. Carmalt, C. J., Neill, S. A. O., Parkin, I. P. & Peters, E. S. Titanium sulfide thin films from the aerosol-assisted chemical vapour deposition of [Ti (SBu t) 4]. *Journal of Materials Chemistry* ***14,*** 830–834 (2004).

30. Kanehori, K., Ito, Y., Kirino, F., Miyauchi, K., & Kudo, T. Titanium disulfide films fabricated by plasma CVD. *Solid State Ionics* ***18,*** 818–822 (1986).

31. Cheon, J., Gozum, J. E. & Girolami, G. S. Chemical Vapor Deposition of MoS2 and TiS2 Films From the Metal - Organic Precursors Mo (S- t -Bu) 4 and Ti (S- t -Bu) 4. *Chemistry of materials* **9**, 1847–1853 (1997).

32. Sherrell, P. C., Sharda, K., Grotta, C., Ranalli, J., Sokolikova, M. S., Pesci, F. M.,

... & Mattevi, C. Thickness-Dependent Characterization of Chemically Exfoliated TiS2 Nanosheets. *ACS Omega* **3**, 8655–8662 (2018).

33. Plashnitsa, V. V., Vietmeyer, F., Petchsang, N., Tongying, P., Kosel, T. H., & Kuno, M. Synthetic strategy and structural and optical characterization of thin highly crystalline titanium disulfide nanosheets. *J. Phys. Chem. Lett.* **3**, 1554–1558 (2012).

34. Mahuli, N. & Sarkar, S. K. Atomic layer deposition of titanium sulfide and its application in extremely thin absorber solar cells. *J. Vac. Sci. Technol. A Vacuum, Surfaces, Film.* **33**, 01A150 (2015).

35. Nam, H., Yang, H., Kim, E., Bae, C. & Shin, H. Semiconducting TiO 2−x S x thin films by atomic layer deposition of TiS2 and its oxidation in ambient . *J. Vac. Sci. Technol. A* **37**, 020916 (2019).

36. Aljabour, A., Coskun, H., Zheng, X., Kibria, M. G., Strobel, M., Hild, S., ... & Stadler, P. Active sulfur sites in semimetallic titanium disulfide enable Co2 electroreduction. *ACS Catal.* **10**, 66–72 (2020).

37. Zang, X., Shen, C., Kao, E., Warren, R., Zhang, R., Teh, K. S., ... & Lin, L. Titanium Disulfide Coated Carbon Nanotube Hybrid Electrodes Enable High Energy Density Symmetric Pseudocapacitors. *Adv. Mater.* **30**, (2018).

38. Basuvalingam, S. B., Zhang, Y., Bloodgood, M. A., Godiksen, R. H., Curto, A. G., Hofmann, J. P., ... & Bol, A. A. Low-Temperature Phase-Controlled Synthesis of Titanium Di- And Tri-sulfide by Atomic Layer Deposition. *Chem. Mater.* **31**, 9354–9362 (2019).

39. Ciatto, G., Chu, M. H., Fontaine, P., Aubert, N., Renevier, H., & Deschanvres, J. L. SIRIUS: A new beamline for in situ X-ray diffraction and spectroscopy studies of advanced materials and nanostructures at the SOLEIL Synchrotron. *Thin Solid Films* **617**, 48–54 (2016).

40. Boichot, R., Tian, L., Richard, M. I., Crisci, A., Chaker, A., Cantelli, V., ... & Renevier, H. Evolution of Crystal Structure During the Initial Stages of ZnO Atomic Layer Deposition. *Chemistry of Materials* **28,** 592-600 (2016).

41. Skopin, E. V., Abdukayumov, K., Abi Younes, P., Anikin, M., Roussel, H., Deschanvres, J. L., & Renevier, H. In situ ellipsometry monitoring of TiO2 atomic layer deposition from Tetrakis (dimethylamido) titanium (IV) and H2O precursors on Si and In 0 . 53 Ga 0 . 47 As substrates. *Thin Solid Films* **723**,

1–8 (2021).

42. Ciatto, G., Aubert, N., Lecroard, M., Engblom, C., Fontaine, P., Dubuisson, J. M., ... & Keller, N. FORTE - a multipurpose high-vacuum diffractometer for tender X-ray diffraction and spectroscopy at the SIRIUS beamline of Synchrotron SOLEIL. *J. Synchrotron Radiat.* **26**, 1374–1387 (2019).

43. Tanuma, S., Powell, C. J. & Penn, D. R. Calculations of electron inelastic mean free paths. IX. Data for 41 elemental solids over the 50 eV to 30 keV range. *Surf. Interface Anal.* **43**, 689–713 (2011).

44. Srivastava, J. K., Prasad, M. & Wagner, J. B. Electrical Conductivity of Silicon Dioxide Thermally Grown on Silicon. *J. Electrochem. Soc*. **132**, 955 (1985).

45. Singh, A., Li, Y., Fodor, B., Makai, L., Zhou, J., Xu, H., ... & Jaramillo, R. Near-infrared optical properties and proposed phase-change usefulness of transition metal disulfides. *Appl. Phys. Lett.* **115**, 161902 (2019).

46. Tauc, J. & Menth, A. States in the gap. *J. Non. Cryst. Solids* **8**–**10**, 569–585 (1972).

47. Van Doorslaer, S., Shane, J. J., Stoll, S., Schweiger, A., Kranenburg, M., & Meier, R. J. Continuous wave and pulse EPR as a tool for the characterization of monocyclopentadienyl Ti(III) catalysts. *J. Organomet. Chem.* **634**, 185–192 (2001).

48. Chu, M. H., Tian, L., Chaker, A., Cantelli, V., Ouled, T., Boichot, R., ... & Ciatto, G. An atomistic view of the incipient growth of zinc oxide nanolayers. *Cryst. Growth Des.* **16**, 5339–5348 (2016).

49. Chu, M. H., Tian, L., Chaker, A., Skopin, E., Cantelli, V., Ouled, T., ... & Ciatto, G. Evaluation of Alternative Atomistic Models for the Incipient Growth of ZnO by Atomic Layer Deposition. *J. Electron. Mater.* **46**, 3512–3517 (2017).

50. Skopin, E. V., Rapenne, L., Roussel, H., Deschanvres, J. L., Blanquet, E., Ciatto, G., ... & Renevier, H. The initial stages of ZnO atomic layer deposition on atomically flat In0.53Ga0.47As substrates. *Nanoscale* **10**, 11585–11596 (2018).

51. Skopin, E. V., Deschanvres, J. L. & Renevier, H. In Situ Ellipsometry Study of the Early Stage of ZnO Atomic Layer Deposition on In0.53Ga0.47As. *Phys. Status Solidi (a),* **217**, (2020).

52. Skopin, E. V., Rapenne, L., Deschanvres, J. L., Blanquet, E., Ciatto, G., Pithan, L., ... & Renevier, H. In situ x-ray studies of the incipient ZnO atomic layer deposition on In0.53Ga0.47As. *Phys. Rev. Mater.* **4**, 1–9 (2020).

53. Wu, Z., Ouvrard, G. & Moreau, P. Interpretation of preedge features in the Ti and S K-edge x-ray-absorption near-edge spectrain the layered disulfides and. *Phys. Rev. B - Condens. Matter Mater. Phys.* **55**, 9508–9513 (1997).

54. Brito, J. L., Ilija, M., & Hernández, P. Thermal and reductive decomposition of ammonium thiomolybdates. *Thermochimica Acta* **256**, 325-338 (1995).

55. Lin, C., Zhu, X., Feng, J., Wu, C., Hu, S., Peng, J., ... & Xie, Y. Hydrogen-incorporated TiS2 ultrathin nanosheets with ultrahigh conductivity for stamp-transferrable electrodes. *J. Am. Chem. Soc.* **135**, 5144–5151 (2013).

56. Dużyńska, A., Judek, J., Wilczyński, K., Zberecki, K., Łapińska, A., Wróblewska, A., & Zdrojek, M. Temperature-induced phonon behavior in titanium disulfide (TiS2) nanosheets. *Journal of Raman Spectroscopy* **50**, 1114–1119 (2019).

57. Hangyo, M., Nakashima, S., Hamada, Y., Nishio, T. & Ohno, Y. Raman scattering from the misfit-layer compounds SnNbS3, PbNbS3, and PbTiS3. *Phys. Rev. B* **48**, 11291–11297 (1993).

58. Ishii, M., Saeki, M., & Kawada, I. Raman Study of Non-Stoichiometric Titanium Sulfides. *physica status solidi (b)* **124,** K109-K112 (1984).

59. Let, A. L., Mainwaring, D. E., Rix, C. & Murugaraj, P. Thio sol-gel synthesis of titanium disulfide thin films and powders using titanium alkoxide precursors. *J. Non. Cryst. Solids* **354**, 1801–1807 (2008).

60. Let, A. L., Mainwaring, D. E., Rix, C. J. & Murugaraj, P. Thio sol-gel synthesis of titanium disulfide thin films and nanoparticles using titanium(IV) alkoxide precursors. *J. Phys. Chem. Solids* **68**, 1428–1435 (2007).

61. Kasai, H., Tolborg, K., Sist, M., Zhang, J., Hathwar, V. R., Filsø, M. Ø., ... & Iversen, B. B. X-ray electron density investigation of chemical bonding in van der Waals materials. *Nat. Mater.* **17**, 249–252 (2018).

62. Martinez, H., Auriel, C., Gonbeau, D. & Loudet, M. Studies of 1T TiS , by STM , AFM and XPS : the mechanism of hydrolysis in air. *Applied surface science* **93**, 0–4 (1996).

63. Fulghum, J. E. Determination of overlayer thickness by angle-resolved XPS: A

comparison of algorithms. *Surf. Interface Anal.* **20**, 161–173 (1993).

64. Dupin, J. C., Gonbeau, D., Martin-Litas, I., Vinatier, P. & Levasseur, A. Amorphous oxysulfide thin films MOySz (M = W, Mo, Ti) XPS characterization: Structural and electronic pecularities. *Applied Surface Science* **173,** 140–150 (2001).

65. Lindic, M. H., Martinez, H., Benayad, A., Pecquenard, B., Vinatier, P., Levasseur, A., & Gonbeau, D. XPS investigations of TiOySz amorphous thin films used as positive electrode in lithium microbatteries. *Solid State Ionics* **176**, 1529–1537 (2005).

66. Lindic, M. H., Pecquenard, B., Vinatier, P., Levasseur, A., Martinez, H., Gonbeau, D., ... & Ouvrard, G. Characterization of rf sputtered TiOySz thin films. *Thin Solid Films* **484**, 113–123 (2005).

67. Dubois, V., Pecquenard, B., Soule, S., Martinez, H. & Le Cras, F. Dual cation- and anion-based redox process in lithium titanium oxysulfide thin film cathodes for all-solid-state lithium-ion batteries. *ACS Appl. Mater. Interfaces* **9**, 2375–2384 (2017).

68. Richard, J., Benayad, A. & Martinet, S. Charge Transfer Mechanism into the Chevrel Phase Mo 6 S 8 during Mg Intercalation. *The Journal of Physical Chemistry C* **121,** 17096-17103 (2017).

69. Martinez, H., Benayad, A., Gonbeau, D., Vinatier, P., Pecquenard, B., & Levasseur, A. Influence of the cation nature of high sulfur content oxysulfide thin films MO y S z (M = W, Ti) studied by XPS. *Appl. Surf. Sci.* **236**, 377–386 (2004).

70. Gonbeau, D., Guimon, C., Pfister-Guillouzo, G., Levasseur, A., Meunier, G., & Dormoy, R. XPS study of thin films of titanium oxysulfides. *Surf. Sci.* **254**, 81–89 (1991).

71. Verner, D. A., Ferland, G. J., Korista, K. T. & Yakovlev, D. G. Atomic Data for Astrophysics. II. New Analytic FITS for Photoionization Cross Sections of Atoms and Ions. *Astrophys. J.* **465**, 487 (1996).

72. Liu, Y., Porter, S. H. & Goldberger, J. E. Dimensional Reduction of a Layered Metal Chalcogenide into a 1D Near-IR Direct Band Gap Semiconductor. *J. Am. Chem. Soc.* **134**, 5044-5047 (2012).

73. Sneh, O. & George, S. M. Thermal stability of hydroxyl groups on a well-

defined silica surface. *J. Phys. Chem.* **99**, 4639–4647 (1995).

74. Coperet, C., Comas-Vives, A., Conley, M. P., Estes, D. P., Fedorov, A., Mougel, V., ... & Zhizhko, P. A. Surface Organometallic and Coordination Chemistry toward Single-Site Heterogeneous Catalysts: Strategies, Methods, Structures, and Activities. *Chem. Rev.* **116**, 323–421 (2016).

75. Roussey, A., Gentile, P., Lafond, D., Martinez, E., Jousseaume, V., Thieuleux, C., & Copéret, C. Cu nanoparticles on 2D and 3D silica substrates: Controlled size and density, and critical size in catalytic silicon nanowire growth. *J. Mater. Chem. C* **1**, 1583–1587 (2013).

76. Mathey, L., Alphazan, T., Valla, M., Veyre, L., Fontaine, H., Enyedi, V., ... & Copéret, C. Functionalization of silica nanoparticles and native silicon oxide with tailored boron-molecular precursors for efficient and predictive p-doping of silicon. *J. Phys. Chem. C* **119**, 13750–13757 (2015).

77. Alphazan, T., Mathey, L., Schwarzwalder, M., Lin, T. H., Rossini, A. J., Wischert, R., ... & Copéret, C. Monolayer Doping of Silicon through Grafting a Tailored Molecular Phosphorus Precursor onto Oxide-Passivated Silicon Surfaces. *Chem. Mater.* **28**, 3634–3640 (2016).

78. Zhuravlev, L. T. The surface chemistry of amorphous silica . Zhuravlev model. *Colloids and Surfaces A: Physicochemical and Engineering Aspects* **173**, 1–38 (2000).

79. Diamond, G. M., Jordan, R. F. & Petersen, J. L. Synthesis of group 4 metal rac-(EBI)M(NR2)2 complexes by amine elimination. Scope and limitations. *Organometallics* **15**, 4030–4037 (1996).

80. Bachrach, S. M., Nguyen, T. T. & Demoin, D. W. Microsolvation of cysteine: A density functional theory study. *J. Phys. Chem. A* **113**, 6172–6181 (2009).

81. Ataman, E., Isvoranu, C., Andersen, J. N., Schnadt, J. & Schulte, K. Unconventional zwitterionic state of l-cysteine. *J. Phys. Chem. Lett.* **2**, 1677–1681 (2011).

82. Mukherjee, A., Sengupta, S. K., Steeves, D. M., Soares, J. W. & Whitten, J. E. Mechanism of thiol-induced color change of tungsten oxide nanoparticles. *Chem. Phys. Lett.* **752**, (2020).

83. Wang, M. & Jiang, X. Sulfur–Sulfur Bond Construction. *Top. Curr. Chem.* **376**, 14 (2018).

1

2

Graphical abstract